Technical University of Denmark

DTU

Numerical simulation of the planar extrudate swell of pseudoplastic and viscoelastic fluids with the streamfunction and the VOF methods

Comminal, Raphaël Benjamin; Pimenta, Francisco; Hattel, Jesper Henri; Alves, Manuel A.; Spangenberg, Jon

Link back to DTU Orbit

DTU Library
Technical Information Center of Denmark

Numerical simulation of the planar extrudate swell of pseudoplastic and viscoelastic fluids with the streamfunction and the VOF methods

Raphaël Comminal[a],[*], Francisco Pimenta[b], Jesper H. Hattel[a], Manuel A. Alves[b], Jon Spangenberg[a]

[a] *Department of Mechanical Engineering, Technical University of Denmark, 2800 Kgs. Lyngby, Denmark*
[b] *CEFT, Department of Chemical Engineering, Faculty of Engineering, University of Porto, 4200-465 Porto, Portugal*

ARTICLE INFO

ABSTRACT

We present an Eulerian free-surface flow solver for incompressible pseudoplastic and viscoelastic non-Newtonian fluids. The free-surface flow solver is based on the streamfunction flow formulation and the volume-of-fluid method. The streamfunction solver computes the vector potential of a solenoidal velocity field, which ensures by construction the mass conservation of the solution, and removes the pressure unknown. Pseudoplastic liquids are modelled with a Carreau model. The viscoelastic fluids are governed by differential constitutive models reformulated with the log-conformation approach, in order to preserve the positive-definiteness of the conformation tensor, and to circumvent the high Weissenberg number problem. The volume fraction of the fluid is advected with a geometric conservative unsplit scheme that preserves a sharp interface representation. For the sake of comparison, we also implemented an algebraic advection scheme for the liquid volume fraction. The proposed numerical method is tested by simulating the planar extrudate swell with the Carreau, Oldroyd-B and Giesekus constitutive models. The swell ratio of the extrudates are compared with the data available in the literature, as well as with numerical simulations performed with the open-source rheoTool toolbox in OpenFOAM®. While the simulations of the generalized Newtonian fluids achieved mesh independence for all the methods tested, the flow simulations of the viscoelastic fluids are more sensitive to mesh refinement and the choice of numerical scheme. Moreover, the simulations of Oldroyd-B fluid flows above a critical Weissenberg number are prone to artificial surface instabilities. These numerical artifacts are due to discretization errors within the Eulerian surface-capturing method. However, the numerical issues arise from the stress singularity at the die exit corner, and the unphysical predictions of the Oldroyd-B model in the skin layer of the extrudate after the die exit, where large extensional deformations occur.

1. Introduction

The simulation of non-Newtonian free-surface flows has a scientific interest, as well as a practical importance in polymer processing. Applications in the plastic industry include the simulations of mold filling in injection molding, profile deformation in extrusion, and 3D printing by fused filament fabrication. The stability of most manufacturing processes for polymers depends on their rheological properties. Non-Newtonian behavior, in general, and viscoelastic effects, in particular, can lead to various processing instabilities [1–4]. Computational fluid dynamics (CFD) simulations can help understanding these instability phenomena and finding the solutions to eliminate them. Moreover, the development of reliable numerical simulations leads to the development of novel computer-aided design strategies in industrial production, using shape optimization algorithms and sensitivity analysis [5–7].

Non-Newtonian materials are characterized by variable viscosities that depend on the flow conditions, i.e. the shear rate or the extensional rate. For instance, molten polymers often exhibit pseudoplastic behavior (shear-thinning). In general, the presence of polymer chains in a fluid enables recoverable deformation, thus, polymeric materials are often viscoelastic. The corollary is that the stress response of the viscoelastic materials depends on the deformation history. In contrast to purely viscous liquids, viscoelastic fluids build up normal stresses in simple shear flows. These normal stresses are responsible for exotic viscoelastic phenomena [8], such as extrudate swell, rod climbing, vortex enhancement, etc. The numerical method presented in this work addresses the simulation of pseudoplastic and viscoelastic non-Newtonian fluid flows with free surfaces. The proposed numerical scheme is tested through simulations of the planar extrudate swell.

The extrudate swell problem was first investigated by Crochet and Keunings [9,10], who developed a Lagrangian finite-element scheme

---

for viscoelastic flows, where the edges of the mesh coincide with the position of the free surfaces. Crochet and Keunings used a conformal mapping of the deformed mesh onto a structured Cartesian grid. Similar approaches were used to solve the extrudate swell of pseudoplastic and viscoplastic fluids [11–13], as well as viscoelastic materials described by various differential and integral constitutive models [14–20]. Automatic adaptive remeshing techniques were later developed in [21,22] to give more flexibility to transient Lagrangian simulations of non-Newtonian free-surface flows when large deformations occur. The arbitrary-Lagrangian–Eulerian method has also been used to simulate the filament stretching [23,24] and extrudate swell [25,26] of viscoelastic liquids. Finally, a few works on the simulation of free-surface viscoelastic flows with the mesh-free smoothed particle hydrodynamics method have been reported in [27–29]. Each of these Lagrangian methods has its own advantages and drawbacks.

In the context of the Eulerian flow representation (where the computational domain is mapped onto a static mesh), the free surfaces are either represented explicitly, with additional geometric objects (e.g. front-tracking with markers or polygons), or implicitly, through an additional field variable (e.g. a level-set function or a color function). Front-tracking methods have been implemented in [30,31] to simulate the deformation of viscoelastic droplets immersed in a Newtonian liquid. Tomé et al. [32] developed a variant of the marker-and-cell method [33] for two- and three-dimensional transient simulations of non-Newtonian free-surface flows, where only the non-Newtonian phase is solved (i.e. the flow of the surrounding air is omitted). This method was used to simulate the extrudate swell and jet buckling phenomena for the generalized Newtonian fluid model [34,35], and for various viscoelastic constitutive models [36–41]. In the level-set method, the position of the interface (or the free surface) is represented with a level-set function that varies continuously across the interface [42]. Hence, the evolution of the level-set function can be solved with implicit advection schemes. The level-set method was used to simulate the ejection of viscoelastic droplets [43] and jet buckling [44]. In the volume-of-fluid (VOF) method, the distribution of the phases is represented by a color function. The discrete counterpart of the color function is the liquid volume fraction inside the control volumes [45]. The VOF method is directly based on the volume conservation, as it essentially solves a transport equation of the color function, either with a geometric scheme or an algebraic scheme. A geometric VOF method was implemented in [46] to simulate various free-surface flows of viscoelastic liquids, in two dimensions. Three-dimensional simulations of viscoelastic jet buckling and filament stretching were achieved with an algebraic VOF scheme in [47]. Free-surface viscoelastic flows have also been simulated using the OpenFOAM® open-source CFD package [48,49]. In addition, a coupled level-set/VOF method was proposed in [50], with the purpose of improving the sharp interface representation and the volume-conservation of free-surface viscoelastic flow solvers. One main advantage of the Eulerian methods is that they can avoid the expensive computations of remeshing, or moving meshes, in contrast with the Lagrangian methods [51].

To the best of our knowledge, all the Eulerian schemes for non-Newtonian free-surface flow simulations are based on velocity-pressure decoupling techniques, like the SIMPLE, PISO, or the fractional-step methods. Most of the Lagrangian schemes are also based on the velocity-pressure formulation, with the notable exception of the work presented in [15,20], which uses the stream-tube method [52,53], where the flow is described in terms of streamfunction and pressure variables. However, the stream-tube method remains difficult to use in flows that contain recirculations [53]. In previous works [54,55], we have shown that a pressure-free *pure streamfunction formulation* [56–60] can also be used to simulate two-dimensional internal viscoelastic flows. The absence of the pressure variable removes the decoupling errors and the time-step size restrictions due to the pressure correction in the classical velocity-pressure algorithms. The numerical scheme presented in [54,55] used the *log-conformation representation* of the viscoelastic

constitutive models, proposed by Fattal and Kupferman [61,62], to tackle the numerical instabilities occurring when the magnitude of the elastic stresses exceeds a critical value. Moreover, a preliminary coupling of the streamfunction formulation with the VOF method was presented in [63], but only for the case of Newtonian two-phase flows.

In the present paper, we propose an Eulerian free-surface flow solver for incompressible generalized Newtonian fluids and viscoelastic fluids, based on the coupling of the pressure-free streamfunction flow formulation, the log-conformation representation, and the VOF method. Two different versions of the VOF method have been implemented: the *Cellwise Conservative Unsplit* (CCU) geometric scheme [64], and the *High Resolution Interface Capturing* (HRIC) algebraic scheme [65]. The performance of the two VOF methods is assessed in the planar extrudate swell problem, where Carreau, Oldroyd-B and Giesekus fluids are tested. The obtained results are also compared with the numerical solutions computed with the open-source *rheoTool* toolbox [66,67], implemented in the finite-volume framework of OpenFOAM® [68], which also uses a VOF surface-capturing algorithm.

The remaining of the paper is organized as follows: the governing equations of the non-Newtonian fluid flows are presented in Section 2, together with a short description of the streamfunction and log-conformation formulations. The discretization of the governing equations and the two versions of the VOF method are detailed in Section 3. The numerical results of the planar extrudate swell problem of the Carreau, Oldroyd-B and Giesekus fluids are reported in Section 4. The capability of the proposed method to predict the extrudate swell is discussed in Section 5. Finally, the main results are summarized in the conclusions section.

2. Governing equations

2.1. Streamfunction flow formulation

The dynamics of the incompressible flow is governed by the conservation of mass and momentum, which can be expressed by the following equations:

$$\nabla \cdot \mathbf{u} = 0, \tag{1}$$

$$\rho \left(\frac{\partial \mathbf{u}}{\partial t} + \mathbf{u} \cdot \nabla \mathbf{u} \right) = -\nabla p + \nabla \cdot \tau, \tag{2}$$

where $\mathbf{u}$ is the velocity field, t is the time, ρ is the density, p is the pressure, and τ is the stress tensor governed by the constitutive models of the material, described in Section 2.2. The two conservation Eqs. (1) and (2) can be reformulated into a single pressure-free governing equation in terms of a vector potential of the velocity field, that is the *stream function*. This reformulation is obtained as follows:

a. The curl operator $\nabla \times$ is applied to the momentum Eq. (2). The curl operation eliminates the pressure gradient from the equations, as $\nabla \times (\nabla p) = \mathbf{0}$, $\forall p \in \mathbb{R}$, which yields the vorticity transport equation:

$$\rho \left(\frac{\partial \omega}{\partial t} + \mathbf{u} \cdot \nabla \omega - \omega \cdot \nabla \mathbf{u} \right) = \nabla \times (\nabla \cdot \tau), \tag{3}$$

where

$$\omega = \nabla \times \mathbf{u} \tag{4}$$

is the vorticity vector.

b. The velocity and vorticity unknowns are expressed in terms of the streamfunction $\boldsymbol{\Phi} \in \mathbb{R}^3$, defined as a vector potential of the velocity field:

$$\mathbf{u} = \nabla \times \boldsymbol{\Phi}. \tag{5}$$

The existence of the streamfunction is guaranteed by the Helmholtz decomposition theorem, provided that **u** is twice continuously differentiable. Moreover, the velocity field is solenoidal due to the incompressibility of the material, expressed in Eq. (1). Further vector calculus manipulations give:

$$\boldsymbol{\omega} = -\nabla^2 \boldsymbol{\Phi}. \tag{6}$$

By replacing all the velocity and vorticity variables inside the vorticity Eq. (3) by their expressions in terms of the streamfunction, using Eqs. (5) and (6), we obtain the following governing equation:

$$\rho \left(\frac{\partial \nabla^2 \boldsymbol{\Phi}}{\partial t} - \nabla \times (\nabla^2 \boldsymbol{\Phi} \times (\nabla \times \boldsymbol{\Phi})) \right) = \nabla \times (\nabla \cdot \boldsymbol{\tau}) \tag{7}$$

that encompasses simultaneously the conservation of mass and momentum.

This reformulation reduces the number of unknowns (as it is pressure-free) and guarantees by construction the mass conservation of the numerical solution, as $\nabla \cdot (\nabla \times \boldsymbol{\Phi}) = 0, \forall \boldsymbol{\Phi} \in \mathbb{R}^3$. It also alleviates time-step restrictions and numerical errors due to the pressure-velocity decoupling. Moreover, it avoids possible competing effects between the pressure and the trace of the stress tensor $\boldsymbol{\tau}$ in the momentum balance, that are believed to degrade the iterative convergence of segregated solvers [54].

The streamfunction formulation is particularly advantageous to describe two-dimensional flows, because planar flows are solely defined by the out-of-plane component of the streamfunction vector; the two other components have trivial solutions. Hence, the two-dimensional streamfunction formulation essentially reduces to a scalar equation. Let for instance a two-dimensional flow be in the xy-plane; then the velocity field is $\mathbf{u} = (\partial \phi / \partial y, -\partial \phi / \partial x, 0)$, where ϕ is the third component of the streamfunction vector $\boldsymbol{\Phi} = (0, 0, \phi)$. The projection of Eq. (7) on the out-of-plane axis $\mathbf{e}_z = \mathbf{e}_x \times \mathbf{e}_y$ gives the scalar equation for ϕ:

$$\rho \left(\frac{\partial \nabla^2 \phi}{\partial t} + \frac{\partial \phi}{\partial y} \frac{\partial \nabla^2 \phi}{\partial x} - \frac{\partial \phi}{\partial x} \frac{\partial \nabla^2 \phi}{\partial y} \right) = [\nabla \times (\nabla \cdot \boldsymbol{\tau})] \cdot \mathbf{e}_z, \tag{8}$$

which describes planar flows.

2.2. Constitutive models

2.2.1. Generalized Newtonian fluid model

The generalized Newtonian fluid model is used as the constitutive law of inelastic materials, where the stress tensor components only depend on the instantaneous local rate of deformation. The generalized Newtonian fluid model provides an algebraic relationship between the constitutive stress tensor $\boldsymbol{\tau}$ and the rate-of-deformation tensor $\mathbf{D} = (\nabla \mathbf{u} + \nabla \mathbf{u}^\mathrm{T})/2$:

$$\boldsymbol{\tau} = 2\eta(\dot{\gamma}) \mathbf{D}, \tag{9}$$

where $\eta(\dot{\gamma})$ is the effective viscosity, which depends on the second invariant of the rate-of-deformation tensor

$$\dot{\gamma} = \sqrt{2\{\mathbf{D} \colon \mathbf{D}\}} = \left(2 \sum_i \sum_j D_{ij} D_{ji} \right)^{1/2}, \tag{10}$$

known as the magnitude of the rate-of-deformation tensor. A constant viscosity η corresponds to the constitutive law of Newtonian fluids. The generalized Newtonian model is very flexible and can describe both pseudoplastic (shear-thinning) and viscoplastic (yield stress) fluids.

In this work, we consider the case of a shear-thinning fluid approaching a power-law constitutive relation. In one-dimensional simple shear flow, the power-law fluids are described by the Ostwald-de Waele law $\tau_{xy} = K(\dot{\gamma}_{xy})^n$, where τ_{xy} and $\dot{\gamma}_{xy}$ are respectively the planar shear stress and shear rate, and K (the fluid consistency) and n (the power-law index) are two material constants. However, a generalization of the Ostwald-de Waele law for arbitrary flows requires special care, as it

yields an infinite viscosity $\eta = \tau_{xy}/\dot{\gamma}_{xy} = K(\dot{\gamma}_{xy})^{n-1}$ in the quiescent state or in a rigid body motion (when $\dot{\gamma}_{xy} = 0$), if $n < 1$. This problem can be avoided with the Carreau fluid model:

$$\eta(\dot{\gamma}) = (\eta_0 - \eta_\infty)(1 + (k\dot{\gamma})^2)^{\frac{n-1}{2}} + \eta_\infty \tag{11}$$

where η_0, η_∞, k and n are material parameters. Using $\eta_\infty = 0$, at large deformation rates (when $k\dot{\gamma} \gg 1$), the Carreau fluid behaves like a power-law fluid with a fluid consistency $K \underset{\dot{\gamma} \gg 1/k}{\simeq} \eta_0 k^{n-1}$ and a power-law index n. However, at low deformation rates (when $k\dot{\gamma} \ll 1$), the Carreau fluid has a plateau viscosity $\eta(\dot{\gamma}) \underset{\dot{\gamma} \to 0}{\simeq} \eta_0$. Parameter k controls the transition between these two constitutive behaviors; its reciprocal $1/k$ corresponds to the critical shear rate where the Carreau fluid shifts between the plateau viscosity and the power-law regions.

The numerical simulations of power-law fluids presented in this paper use Carreau fluid models with very large plateau viscosity η_0 and parameter k. The plateau viscosity serves as the cut-off value of the viscosity, when the power-law fluid is close to the quiescent state. In addition, the k parameter is chosen according to the power-law index, such that all the Carreau models, with different values of n, give the same apparent viscosity $\eta(\dot{\gamma}_c)$ at the characteristic shear rate of the flow.

For instance, the choice $\eta_0 = 10^5 \eta(\dot{\gamma}_c)$ and $k = \frac{(\eta(\dot{\gamma}_c)/\eta_0)^{\frac{1}{n-1}}}{\dot{\gamma}_c}$ guarantees that the critical shear rate $1/k$ of the Carreau model (below which the power-law viscosity transitions to the plateau value) remains lower than $10^{-5} \dot{\gamma}_c$, for any power-law index $0 < n < 1$. Hence, the Carreau model can provide very good approximations of power-law fluids.

2.2.2. Oldroyd-B model

The Oldroyd-B model [69] describes the linear behavior of a viscoelastic fluid under small deformation rates. The original Oldroyd-B model reads:

$$\boldsymbol{\tau} + \lambda \overset{\triangledown}{\boldsymbol{\tau}} = 2\eta \left(\mathbf{D} + \lambda_r \overset{\triangledown}{\mathbf{D}} \right), \tag{12}$$

where η is the viscosity of the fluid, λ is the relaxation time, $\lambda_r < \lambda$ is the retardation time, and $\overset{\triangledown}{\cdot}$ denotes the upper-convected time-derivative, defined in Eq. (17). For numerical simulations, it is convenient to split the stress tensor into the solvent and the polymer contributions [70]:

$$\boldsymbol{\tau} = \boldsymbol{\tau}_\mathrm{S} + \boldsymbol{\tau}_\mathrm{P}, \tag{13}$$

where

$$\boldsymbol{\tau}_\mathrm{S} = 2\beta\eta \mathbf{D} \tag{14}$$

is the instantaneous (purely viscous) solvent stress response, and $\boldsymbol{\tau}_\mathrm{P}$ is the memory-dependent (viscoelastic) polymeric extra-stress contribution. The polymeric component of the stress tensor is related to a conformation tensor **c** representing the internal elastic strain of the liquid:

$$\boldsymbol{\tau}_\mathrm{P} = \frac{(1-\beta)\eta}{\lambda}(\mathbf{c} - \mathbf{I}), \tag{15}$$

where $G = (1-\beta)\eta/\lambda$ is the elastic modulus and **I** the identity tensor. The material parameter $\beta = \lambda_r/\lambda$ is the retardation parameter (also called the solvent viscosity ratio) that controls the fraction of the viscosity contributing to the instantaneous (solvent) and the memory-dependent (polymeric) stress responses. The physical-admissibility of the extra-stress tensor requires the conformation tensor to be symmetric positive definite. For the Oldroyd-B model, the conformation tensor is governed by the following differential equation:

$$\overset{\triangledown}{\mathbf{c}} = -\frac{1}{\lambda}(\mathbf{c} - \mathbf{I}), \tag{16}$$

where the upper-convected time-derivative

$$\overset{\triangledown}{\mathbf{c}} \equiv \frac{\partial \mathbf{c}}{\partial t} + \mathbf{u} \cdot \nabla \mathbf{c} - (\mathbf{c} \cdot \nabla \mathbf{u}^{\mathrm{T}} + \nabla \mathbf{u} \cdot \mathbf{c}) \tag{17}$$

accounts for the material transport and the frame-invariance of the conformation tensor. In Einstein notation, the velocity gradient used throughout this work refers to $(\nabla \mathbf{u})_{ij} = \partial u_i / \partial x_j$. The right-hand side term in Eq. (16) is responsible for the growth and the relaxation of the internal elastic strain of the linear viscoelastic fluid. The relative magnitude of the elastic stresses as compared to the viscous stresses is quantified by the dimensionless *Weissenberg number*:

$$Wi = \lambda \dot{\gamma}_c. \tag{18}$$

The Oldroyd-B model can also be derived from the kinetic theory of Kramers [71], assuming that polymer molecules behave like a suspension of linear elastic dumbbells diluted in a Newtonian solvent and subjected to the Brownian motion. Thus, the Oldroyd-B model is a first approximation of the viscoelastic behavior of dilute polymer solutions flowing under low shear rates. It predicts basic viscoelasticity features such as stress relaxation, creep deformations and a quadratic first normal stress difference in viscometric flows. However, it does not describe shear-thinning, and it gives an unrealistic representation of the extensional viscosity, because of the absence of a mechanism to limit the elongation of the linear spring connecting the dumbbells. Indeed, the Oldroyd-B model can give rise to an infinite stress growth in extensional flows when $\dot{\varepsilon} \geq 0.5/\lambda$. Despite these drawbacks, the Oldroyd-B model remains useful to test the stability of numerical methods and to reproduce, at least qualitatively, several viscoelastic phenomena.

2.2.3. Single-mode Giesekus model

Giesekus proposed the concept of configuration-dependent tensorial molecular mobility [72] to take into account the intermolecular polymer-polymer interactions, which are ignored in the Oldroyd-B model. The molecular mobility tensor emerges from the dumbbells kinetic model with an anisotropic hydrodynamic drag and anisotropic Brownian motions [73]. Giesekus postulated a linear dependency of the mobility tensor on the conformation tensor, and derived the following constitutive equation [74]:

$$\overset{\triangledown}{\mathbf{c}} = -\frac{1}{\lambda}(\mathbf{I} + \alpha(\mathbf{c} - \mathbf{I}))(\mathbf{c} - \mathbf{I}), \tag{19}$$

where $0 \leq \alpha \leq 0.5$ is the dimensionless mobility parameter quantifying the degree of anisotropy. In the special case $\alpha = 0.5$, the Giesekus model describes the reptation motion of entangled long polymer chains, while for $\alpha = 0$, the model is isotropic and reduces to the Oldroyd-B model. The Giesekus model (for $\alpha > 0$) predicts shear-thinning and a bounded stress growth in extensional flows. Moreover, it fits qualitatively well the rheometric measurements of unbranched polymer melts, both in shear and uniaxial extensional experiments [75], although it has a single adjustable non-linear parameter (α). The steady-state material functions of the Giesekus fluid model are represented in Fig. 1 (the shear viscosity and the first normal stress coefficient are provided in [8], p. 368; the planar extensional viscosity was calculated numerically). The limiting case $\alpha = 0$ corresponds to the Oldroyd-B model. As it can be seen in Fig. 1(a) and (b), the Giesekus fluid model (for $\alpha \neq 0$) presents shear-thinning both for the steady shear viscosity $\eta \equiv \tau_{xy}(\dot{\gamma}_{xy})/\dot{\gamma}_{xy}$, and the steady first normal stress difference coefficient $\psi_1 \equiv (\tau_{xx} - \tau_{yy})/\dot{\gamma}_{xy}^2 = N_1(\dot{\gamma}_{xy})/\dot{\gamma}_{xy}^2$, for a simple shear flow in the *xy*-plane. Moreover, the Giesekus fluid model has a finite planar extensional viscosity, except in the case $\alpha = 0$ corresponding to the Oldroyd-B fluid model where the steady planar extensional viscosity becomes infinite when $\dot{\varepsilon} \geq 0.5/\lambda$; see Fig. 1(c).

2.3. Log-conformation representation

Differential viscoelastic models like the Oldroyd-B and the Giesekus constitutive equations are generally prone to numerical instabilities
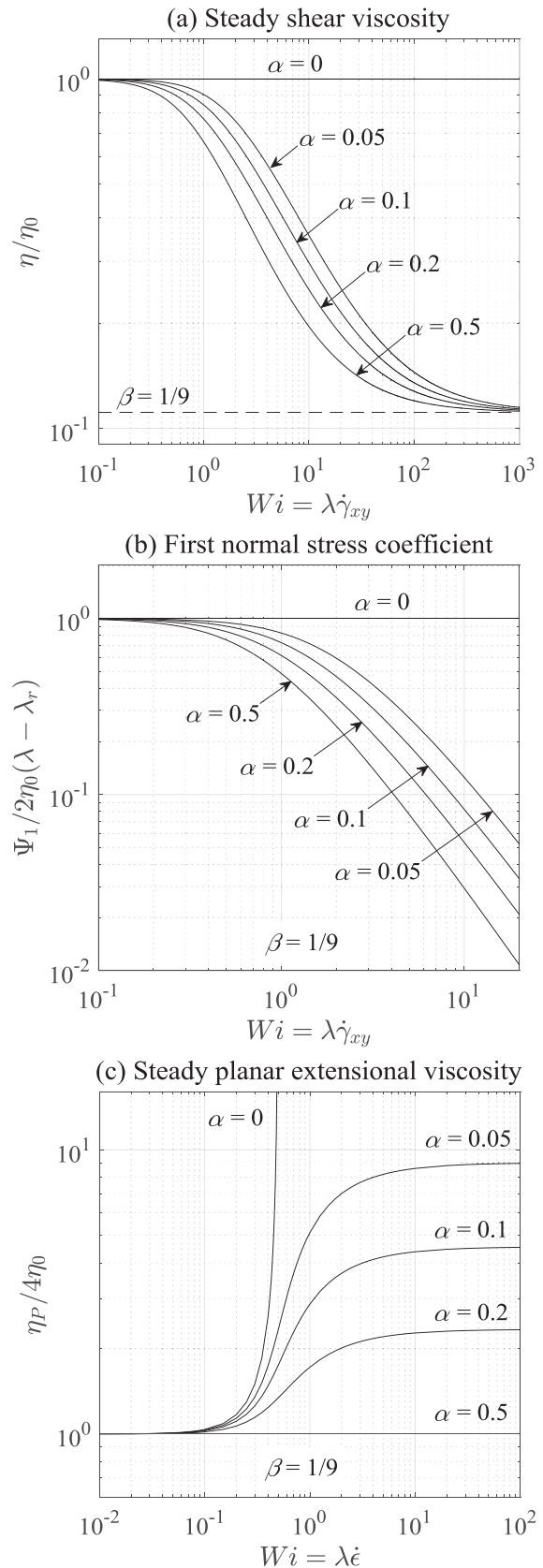

Fig. 1. Normalized steady-state material functions of the Giesekus model, for $\beta = 1/9$: (a) steady shear viscosity, (b) first normal stress difference coefficient, and (c) steady planar extensional viscosity. The limiting case $\alpha = 0$ corresponds to the Oldroyd-B model.

when the Weissenberg number exceeds a critical value, depending on the flow, the numerical scheme, and the mesh. For the Oldroyd-B model, the critical Weissenberg number is typically of the order one. This phenomenon of numerical instability is referred to in the literature as the *high Weissenberg number problem*. This numerical issue comes both from the deficiency of many of the constitutive models (and the Oldroyd-B model in particular) to predict realistic stresses at large extensional strain rates, and the inability of the numerical methods to represent stress gradients accurately. Indeed, the Oldroyd-B model can predict unbounded stress growth under finite extensional rates. Thus, the solution may contain stress singularities with exponential or non-smooth stress profiles near salient corners of the geometry and stagnation points [67,76,77]. Moreover, the numerical approximation of exponential stress profiles with finite differences or finite elements is prone to numerical errors. Hulsen et al. [78] explained that the underestimation of the stress gradient in Eq. (17) is numerically compensated by an over-estimation of the stress growth-rate in Eq. (16), which favors an accumulation of numerical errors. The numerical scheme eventually breaks down when the conformation tensor loses its positive-definiteness property (due to accumulated numerical errors), leading to unphysical stress states, and ultimately to the simulation blowup.

The high Weissenberg number problem was tackled by the log-conformation representation of the differential constitutive models, which enforces by construction the positive-definiteness of the conformation tensor. The constitutive model, Eq. (16), is reformulated with a change of variable in terms of the matrix-logarithm of the conformation tensor:

$$\boldsymbol{\Psi} = \log(\mathbf{c}). \tag{20}$$

The matrix-logarithm of $\mathbf{c}$ requires its eigen-decomposition following the methodology described in [61,62]. In addition, the velocity gradient is decomposed as follows:

$$\nabla \mathbf{u} = \mathbf{E} + \boldsymbol{\Omega} + \mathbf{N}\mathbf{c}^{-1}, \tag{21}$$

where $\mathbf{E}$ is symmetric and traceless, $\boldsymbol{\Omega}$ is anti-symmetric, and $\mathbf{N}$ is an anti-symmetric matrix that commutes with $\mathbf{c}$ [61]. Finally, the log-conformation representation of the differential viscoelastic models yields the following evolution equation for the matrix-logarithm of the conformation tensor [61]:

$$\frac{\partial \boldsymbol{\Psi}}{\partial t} + \mathbf{u} \cdot \nabla \boldsymbol{\Psi} - (\boldsymbol{\Omega}\boldsymbol{\Psi} - \boldsymbol{\Psi}\boldsymbol{\Omega}) - 2\mathbf{E} = \frac{1}{\lambda} \boldsymbol{f}_R(\boldsymbol{\Psi}), \tag{22}$$

where

$$\boldsymbol{f}_R(\boldsymbol{\Psi}) = \begin{cases} \exp(-\boldsymbol{\Psi}) - \mathbf{I} & \text{Oldroyd-B model} \\ -\alpha \exp(\boldsymbol{\Psi}) + (1-\alpha)\exp(-\boldsymbol{\Psi}) & \text{Giesekus model} \\ \quad + (2\alpha - 1)\mathbf{I} \end{cases} \tag{23}$$

is the relaxation function of the constitutive model in terms of $\boldsymbol{\Psi}$. Contrary to the original formulation, the exponential stress profiles are linearized by the log-conformation change of variable, Eq. (20). Once the evolution Eq. (22) is solved, the conformation tensor is recovered via the inverse operation

$$\mathbf{c} = \exp(\boldsymbol{\Psi}), \tag{24}$$

which guarantees by construction the positive-definiteness of $\mathbf{c}$, irrespectively of numerical errors in the solution of $\boldsymbol{\Psi}$. Finally, the conformation tensor is used to compute the curl of the divergence of the extra-stress tensor $\nabla \times (\nabla \cdot [(1-\beta)\eta(\mathbf{c} - \mathbf{I})/\lambda])$, which appears as a source term in the streamfunction flow formulation, Eq. (7).

3. Numerical method

3.1. Overview of the algorithm

The free-surface flows of non-Newtonian fluids are modelled as

immiscible two-phase flows, within the Eulerian framework, where the secondary fluid phase represents the surrounding air. The Eulerian description of the flow field provides a robust and flexible framework to handle potential changes in the topology of the free surfaces, as for instance the merging of flow fronts or the breakup of thin films or filaments of fluids occurring in polymer processing. The surrounding air is assumed to flow as an incompressible Newtonian fluid, while the primary phase of the non-Newtonian liquid obeys one of the constitutive models described in Section 2.2. In addition, unless otherwise stated, the convective terms in the momentum (and the streamfunction) equations are neglected in both fluid phases; hence, the Reynolds number is $Re = 0$, representative of creeping flow.

The calculation domain is meshed with a non-uniform Cartesian grid. The grid forms the control volumes that are used to discretize the governing equations of the discrete unknowns with the finite-volume method. The discrete components of the extra-stress and the log-conformation tensors (for viscoelastic fluids) are cell-centered with respect to the Cartesian grid, while the discrete velocity variables are face-centered, forming staggered control volumes. Finally, pointwise streamfunction unknowns are located at the intersections of the grid lines; see Fig. 2. The streamfunction equations, and the log-conformation equations (for the viscoelastic fluids), are discretized with the implicit numerical schemes described in Section 3.2; see also [54,55] for more details. The streamfunction and the log-conformation tensors are computed sequentially with successive substitution iterations, until iterative convergence is reached. The absence of pressure unknowns (due to the streamfunction formulation) facilitates the convergence of the iterative algorithm.

The free-surfaces are advected explicitly with the VOF method, at the end of each time-step, once the iterative streamfunction/log-conformation solver has reached convergence. The VOF method directly solves the volume conservation of the fluid phases. The distribution of the non-Newtonian liquid inside the two-phase flow is represented through the color function $\chi(\mathbf{x}, t)$, defined as:

$$\chi(\mathbf{x}, t) = \begin{cases} 1 & \text{in the non-Newtonian liquid,} \\ 0 & \text{in the surrounding air.} \end{cases} \tag{25}$$

The discrete counterpart of the color function is the liquid volume fraction θ (of the non-Newtonian phase), calculated as the volume-average of $\chi(\mathbf{x}, t)$, inside each cell of the mesh:
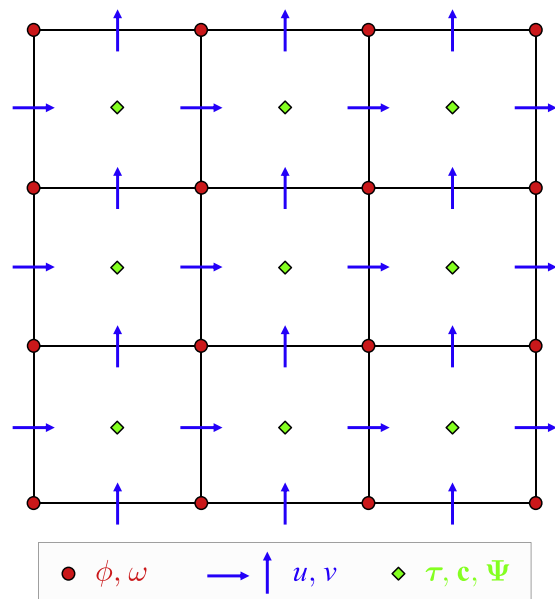
Fig. 2. Staggered arrangement of the discrete variables on the Cartesian grid.

$$\theta = \frac{1}{V_\Omega} \int_\Omega \chi(\mathbf{x}, t) dV, \tag{26}$$

where $V_\Omega = \int_\Omega dV$ is the total volume of the grid cell Ω. As the color function is advected with the flow, the liquid volume fraction is governed by a transport equation. Two approaches have been tested in this work to solve the transport equation of the liquid volume fraction: the geometric VOF method with sharp interface representation, and the algebraic advection method which smears the interface location; see more details in Section 3.3.

The material properties inside the control volume containing a mixture of the two phases (where $0 < \theta < 1$) are averaged using the arithmetic rule of mixture:

$$\eta = \theta\eta_1 + (1 - \theta)\eta_2,$$
$$\rho = \theta\rho_1 + (1 - \theta)\rho_2, \tag{27}$$

where indices 1 and 2 refer to the pure material properties of phase 1 (the non-Newtonian fluid) and phase 2 (surrounding air), respectively. If the non-Newtonian fluid is viscoelastic, the elastic modulus of the mixture is averaged as

$$G = \theta G_1. \tag{28}$$

The relaxation time and the viscosity ratio in the constitutive equations of the interfacial cells are unchanged. The diagram in Fig. 3 gives an overview of the in-house CFD code that we developed, based on the streamfunction/log-conformation formulations and the VOF methods.
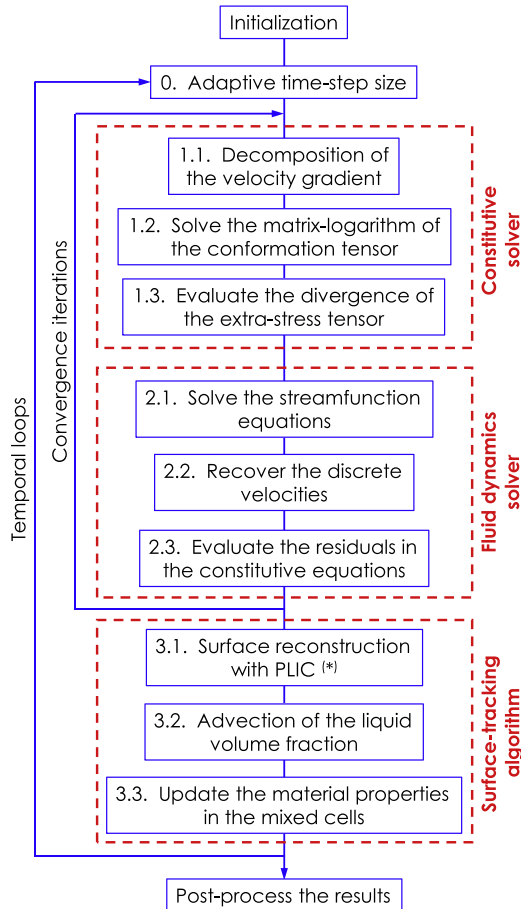

Fig. 3. Overview of the in-house CFD code. [*] The surface reconstruction (step 3.1) is only applicable for the geometric VOF algorithm, e.g. with the CCU scheme.

3.2. Discretization of the governing equations

This subsection discusses the discretization of the streamfunction and log-conformation partial-differential equations governing the dynamics of the flow, with the finite-volume method. We have essentially used the same discretization scheme as the one proposed in [54], for single-phase viscoelastic fluid flows. In order to discretize the streamfunction equations, we first discretize the momentum equations (3) and the curl operators in Eqs. (4) and (5). Let the linear system of the discretized momentum equations be:

$$[\mathbf{A}]\{\mathbf{u}\} = \{\mathbf{b}\}, \tag{29}$$

where $[\mathbf{A}]$ is the Jacobi matrix of the system of equations, $\{\mathbf{u}\}$ is the vector of the discrete velocity unknowns, and $\{\mathbf{b}\}$ is the right-hand side of the system of equations, containing the terms that are discretized explicitly. Now, let $[\mathbf{R}]$ be the discrete curl operator that links $\{\mathbf{u}\}$ to the vector of the discrete vorticities $\{\boldsymbol{\omega}\}$, and $[\mathbf{C}]$ be the discrete curl operator that links the vector of the discrete streamfunctions $\{\boldsymbol{\Phi}\}$ to $\{\mathbf{u}\}$:

$$\{\boldsymbol{\omega}\} = [\mathbf{R}]\{\mathbf{u}\}, \tag{30}$$

$$\{\mathbf{u}\} = [\mathbf{C}]\{\boldsymbol{\Phi}\}. \tag{31}$$

The discretization of the curl operators $[\mathbf{R}]$ and $[\mathbf{C}]$ with finite differences is described in [79]. The streamfunction reformulation presented in Section 2.1 is applied at the discrete level. Thus, the linear system of the discretized streamfunction equation is obtained by substituting the matrix relation (31) inside the equation system (29) and multiplying the result by $[\mathbf{R}]$ on the left, yielding the following matrix relation:

$$[\mathbf{R}][\mathbf{A}][\mathbf{C}]\{\boldsymbol{\Phi}\} = [\mathbf{R}]\{\mathbf{b}\}. \tag{32}$$

Hence, the matrix product $[\mathbf{R}][\mathbf{A}][\mathbf{C}]$ is the Jacobi matrix of the discretized system of streamfunction equations, and the matrix-vector product $[\mathbf{R}]\{\mathbf{b}\}$ is the right-hand side.

The diffusive fluxes in the discrete momentum equations (arising from the purely viscous stresses, $2\eta(\dot{\gamma})\mathbf{D}$ for the generalized Newtonian fluid, and $2\beta\eta\mathbf{D}$ for the viscoelastic fluid) are discretized by finite differences, taking advantage of the staggered arrangement of the discrete velocities; see details in [54]. With the streamfunction formulation, and the solvent-polymeric stress splitting formulation, Eq. (13), the curl of the purely viscous stress yields a bi-harmonic term of the streamfunction $\nabla \times (\nabla \cdot \tau_S) = \beta\eta\nabla^4\boldsymbol{\Phi}$, which enhances the ellipticity of the flow formulation, and improves the numerical stability.

The convective fluxes in the log-conformation equations are evaluated component-wise with the CUBISTA high-resolution advection scheme [80], which was specially designed for the simulations of viscoelastic fluids. Moreover, the upwind deferred-correction approach [81] is adopted to enhance numerical stability: the upwind component of the scheme is discretized implicitly, while the remaining higher-order terms are discretized explicitly. The numerical procedure to perform the change of variable between the conformation tensor and its matrix-logarithm, as well as the decomposition of the velocity gradient tensor, in the two-dimensional case, is detailed in the original publication of Fattal and Kupferman [61].

The shear components of the extra-stress tensor are linearly interpolated from cell centers to the vertices of the grid intersections, for the discretization of the divergence of the extra-stress tensor, in the momentum equations. Finally, the time-derivatives are discretized with the two-level backward differentiation formula [54].

3.3. Free-surface tracking with the VOF method

As mentioned earlier, the family of the VOF method used in this work can be divided into two branches, depending on whether the liquid volume fraction is advected with a geometric method or an

3.3.1. Geometric advection scheme

The VOF method originally proposed by Hirt and Nichols [82] was a geometric scheme, using a simple line interface calculation and the donor-acceptor advection scheme. Geometric VOF methods require two procedures: first, a reconstruction of the interface, based on the distribution of the liquid volume fractions; secondly, an advection scheme consisting in the evaluation of either the donating-regions of the fluxes (edgewise approach) or the pre-images of the cells (cellwise approach), by a semi-Lagrangian backward tracing of the flow pathlines during the time-step. Both advection approaches are theoretically equivalent [83]. However, in practice, the cellwise approach handles with more simplicity the cases where the liquid volume travels through several grid cells within a single time-step. These types of methods are described as *geometric* because the update of the liquid volume fractions involves calculations of polygonal intersections between the donating-regions/ pre-images and the reconstructed interfaces.

The interface is reconstructed with the PLIC (Piecewise Linear Interface Calculation) representation, which is standard for the geometric VOF methods [45]. In the PLIC representation, the interface is represented inside each grid cell by the line equation:

$$\hat{\mathbf{n}}\cdot\mathbf{x} + d = 0, \tag{33}$$

where $\hat{\mathbf{n}}$ is the normal vector of the interface (pointing outward to the liquid), d is the signed distance of the line to the cell's origin, and $\mathbf{x}$ is the position of the points that belong to the line. In this work, the normal vector of the interface was computed with the least-squares ELVIRA algorithm [84].

Concerning the advection schemes, the geometric VOF methods divide into directional-split and unsplit (multi-dimensional) schemes. The unsplit advection schemes are generally more accurate (less numerical diffusion) than the directional-split advection schemes. Moreover, unsplit advection schemes can be designed to be bounded and conservative. Nevertheless, these schemes are more complex to implement in three dimensions, and for arbitrary meshes. Indeed, general three-dimensional unsplit geometric advection schemes possessing the boundedness and conservativeness properties have only been derived recently [85–87]. In this work, we use the CCU advection scheme [64], which is also bounded and conservative, but limited to two-dimensional problems. The CCU scheme traces backward in time the pre-image of the grid cells, with a fourth-order Runge-Kutta method and bi-cubic spatial interpolations of the intermediate velocities. By definition, the liquid volume inside a cell's pre-image will be entirely contained in this cell, at the next time-step. With the CCU scheme, the pre-images of the Cartesian grid cells are represented by 8-vertex polygons. Fig. 4 represents the 8-vertex pre-image polygon *ABCDEFGH* of a grid cell *ijkl*. The liquid volume of this grid cell is updated by the liquid volume of its pre-image, which corresponds to the area of the pre-image polygon truncated by the reconstructed interface. The boundedness and conservativeness of the geometric VOF advection schemes require certain conditions: (i) that the volume of each pre-image polygon equals the volume of its original cell, (ii) the pre-images of the different cells do not overlap, and (iii) the pre-images of adjacent grid cells share common edges that coincide with each other [64].

3.3.2. Algebraic advection scheme

The algebraic VOF schemes directly solve the transport equation of the color function

$$\frac{\partial \chi}{\partial t} + \nabla\cdot(\mathbf{u}\chi) = 0, \tag{34}$$

which is discretized into the advection equation of the liquid volume fraction θ, once integrated over the control volumes with the finite-volume method. Thus, the algebraic VOF schemes can be easily coupled with existing finite-volume solvers. Moreover, their extension from two-
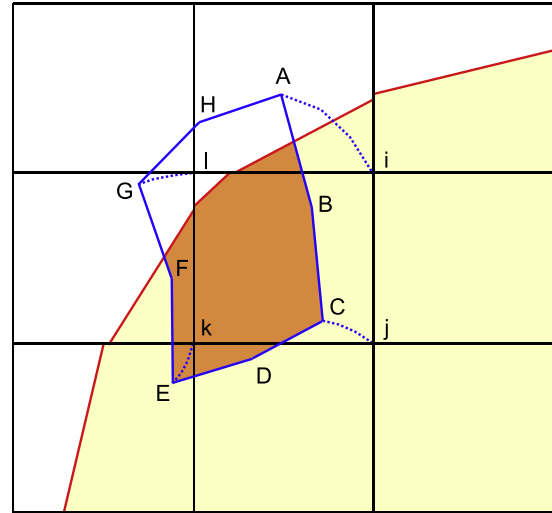

Fig. 4. Backward tracing of the liquid volume with the CCU scheme. The polygon *ABCDEFGH* is the pre-image of the grid cell *ijkl*. The dotted lines are the streaklines of flow passing through the vertices of the grid cell, during the time-step. The PLIC reconstruction is represented by the red segments. The liquid volume of the grid cell is updated by the intersection of the pre-image polygon with the PLIC (i.e. the dark colored area). (For interpretation of the references to colour in this figure legend, the reader is referred to the web version of this article.)

dimensional cases to three-dimensional problems, as well as their implementation on unstructured meshes, do not present the same difficulty as for geometric VOF schemes. Nevertheless, the inherent numerical diffusion due to the discretization of Eq. (34) smooths the jump of the color function across the interface. Thus, the position of the interface, which is defined by the iso-value $\theta = 0.5$ of the liquid volume fraction, loses its compactness and becomes smeared over a few layers of control volumes. The inevitable discretization errors also affect the volume-conservation of the advection schemes. Hence, the overall accuracy of the algebraic VOF schemes degrades over the simulation time.

The accuracy and the stability of the algebraic VOF method depend on the choice of the interpolation scheme that is used to estimate the fluxes of the liquid volume through the faces of the control volume. Moreover, it is the volume flux calculation that distinguishes the different algebraic VOF schemes, see for instance [65,88–90]. There is no single ideal interpolation scheme for the volume fluxes, as the high-order accuracy often comes at the expense of the physical-boundedness of the liquid volume, which requires that $0 \leq \theta \leq 1$.

In this work, we use the HRIC algebraic scheme [65], which is based on a blending of the upwind differencing scheme (UDS) and the downwind differencing scheme (DDS). On the one hand, the UDS scheme is unconditionally stable, but it produces large numerical diffusion, which degrades the precision of the free-surface capturing. On the other hand, the DDS scheme introduces a "negative numerical diffusion" which maintains the compactness of the interface, but also results in an artificial compressibility of the liquid volume (impacting the volume-conservation). Moreover, both the UDS and the DDS schemes have the advantage of being physically bounded ($0 \leq \theta \leq 1$). The HRIC advection scheme strives to combine both advantages of the UDS and the DDS schemes. The HRIC scheme interpolates the flux of the liquid volume θ_f through face f between two control volumes, as a function of the liquid volume in the upwind and downwind cells, θ_U and θ_D, respectively. In terms of the Normalized Variable Diagram (NVD) [91], the HRIC scheme computes θ_f according to the following composite scheme:

$$\tilde{\theta}_f = \begin{cases} \tilde{\theta}_U & \text{for } \tilde{\theta}_U < 0, \ \tilde{\theta}_U > 1 \ (\text{UDS}) \\ 2\tilde{\theta}_U & \text{for } 0 \leq \tilde{\theta}_U < 1/2 \quad (\text{linear combination}) \\ 1 & \text{for } 1/2 \leq \tilde{\theta}_U \leq 1 \quad (\text{DDS}) \end{cases} \tag{35}$$

Table 1
Summary of the three numerical methodologies tested.

Numerical schemes:	I	II	III
Code:	In-house CFD code	In-house CFD code	RheoTool in OpenFOAM®
Incompressible flow solver:	Pure streamfunction formulation	Pure streamfunction formulation	SIMPLEC velocity-pressure coupling algorithm
Viscoelastic stress solver:	Log-conformation representation	Log-conformation representation	Log-conformation representation
VOF solver:	Geometric CCU scheme, PLIC reconstruction	Algebraic HRIC scheme	Algebraic MULES

where

$$\tilde{\theta}_f = \frac{\theta_f - \theta_{UU}}{\theta_D - \theta_{UU}}, \quad \tilde{\theta}_U = \frac{\theta_U - \theta_{UU}}{\theta_D - \theta_{UU}} \tag{36}$$

are the normalized values of the liquid volume at the face f and inside the upwind cell, respectively. The value θ_{UU} in Eq. (36) refers to the liquid volume fraction in the second upwind cell relative to face f.

The original HRIC scheme further blends the interpolated values given by the scheme (35), with the UDS scheme, when the interface is not parallel to the cell's face, and when the local Courant number exceeds the threshold value 0.3. These corrections to the interpolated flux of the liquid volume aim at avoiding an artificial alignment of the interface with the numerical grid, as well as convergence issues. However, we did not notice such problems in our advection tests. Thus, we retained the interpolated values of liquid volume provided in Eq. (35). Moreover, we imposed a maximum Courant number below the threshold value 0.3 in all our simulations of planar extrusion.

3.4. Numerical settings in rheoTool

In order to have a basis of comparison to assess the accuracy and robustness of the method developed, additional simulations were also conducted in the open-source *rheoTool* toolbox [66], available for the OpenFOAM® library. For this purpose, we used the *rheoInterFoam* solver, which couples the solver originally developed for single-phase flows [66] with the algebraic VOF method of OpenFOAM® [92], thus enabling the simulation of two-phase flows of complex fluids. The code is generic for 2D/3D geometries and it allows the use of polyhedral meshes. A number of constitutive models can be assigned individually to each phase, and it is also possible to take into account surface tension effects [66]. The pressure-velocity coupling is assured by the SIMPLEC algorithm [93], and the stresses are evaluated using the log-conformation representation. The details of the stress-velocity coupling were presented in [67]. In the algebraic VOF method available in OpenFOAM®, the color function is advected explicitly through the Multidimensional Universal Limiter with Explicit Solution (MULES) method, which introduces a compressive flux in the interface between the phases in order to minimize diffusion effects [92]. Importantly, the extra-stresses are computed in a different way comparing to the in-

house code here described. A constitutive equation is solved separately for each phase, using its corresponding material properties (e.g. the relaxation time and the retardation parameter). Then, the cell-averaged extra-stresses are evaluated by weighting arithmetically the extra-stress tensor of each phase, using the liquid volume fractions as weighting coefficients [66]. When one of the phases is inelastic, its contribution to the polymeric extra-stresses is null, and no constitutive equation is solved. In addition to this, other differences exist between the *rheoInterFoam* solver and the in-house code, some of which are the variables arrangement on the grid (staggered in the in-house code versus collocated in *rheoInterFoam*), the pressure-velocity coupling (streamfunction formulation in the in-house code versus the SIMPLEC method in *rheoInterFoam*) and the VOF method (CCU or HRIC in the in-house code versus MULES in *rheoInterFoam*).

The convective terms were discretized using the CUBISTA high-resolution scheme, and time-derivatives were evaluated with the first-order Euler method. The compressive flux in the MULES method was computed using the parameter $C_\alpha = 1$, to restrict interface smearing (see details in [92]). The simulations with *rheoTool* were run for a constant Reynolds number, $Re = 0.01$, which is also representative of creeping flow conditions.

4. Planar extrusion simulation

The numerical schemes described in Sections 3.1–3.3 were implemented in an in-house CFD code [54] and tested in the simulation of the planar extrusion of the Carreau, Oldroyd-B and Giesekus fluids. The code is based on the streamfunction/log-conformation formulation. In addition, two versions of the VOF method were implemented: one with the CCU geometric scheme (I), and the other with HRIC algebraic scheme (II). The planar extrusion was also simulated with the *rheoTool* toolbox (III). The three different numerical methodologies are summarized in Table 1.

The geometry of the planar extrusion simulations consists in a narrow rectangular channel (representing an extrusion die) that opens on a wider rectangular expansion region; see Fig. 5. A symmetry boundary condition is applied on plane $y = 0$ to reduce the computational cost. The half-width h of the narrow channel is used as the characteristic length scale. Both the narrow channel and the wider
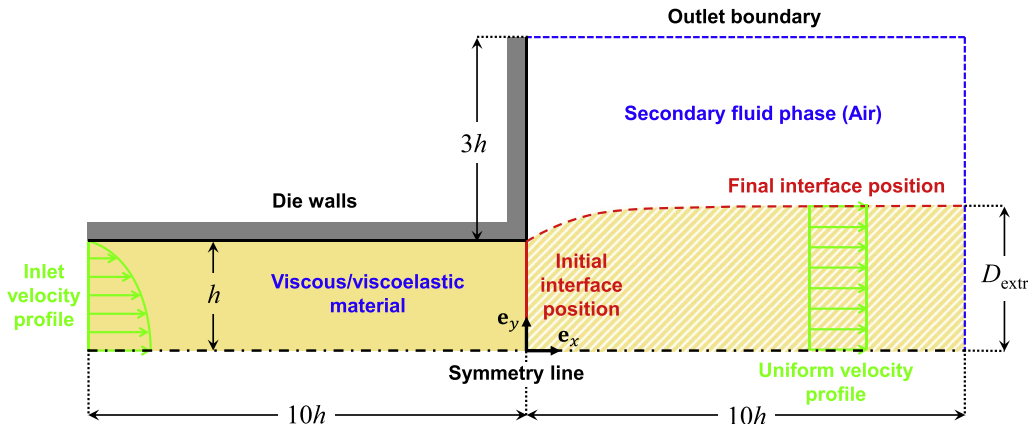

Fig. 5. Geometry of planar extrudate swell problem.

expansion region have the same length, $10h$. The expansion region has a width $3h$, which is large enough to not influence the flow dynamics.

The no-slip boundary condition is applied at the walls. A fully-developed velocity profile is applied as boundary condition at the entry of the narrow channel, while the outer periphery of the expansion region is assigned an outlet Neumann boundary condition. At the initial time, the narrow channel is already filled with the non-Newtonian liquid, such that the initial position of the interface coincides with the expansion plane; see Fig. 5. The transient extrusion is simulated during a total time $T = 90/\dot{\gamma}_w$, where $\dot{\gamma}_w = 3\overline{U}/h$ is the wall shear rate of the planar Poiseuille flow of a Newtonian fluid (used as characteristic shear rate), and $\overline{U}$ is the average velocity at the inlet. The second phase representing the air is modeled as a Newtonian fluid with very low density and viscosity, such that $\rho_{\text{air}} = 10^{-2}\rho$, $\eta_{\text{air}} = 10^{-11}\eta_0$ for the Carreau fluids, and $\eta_{\text{air}} = 10^{-6}\beta\eta$ for the viscoelastic fluids (note that the properties used do not match those of air, but are representative of a low viscosity and low density fluid).

The simulations were performed on three non-uniform Cartesian grids, M1 (coarse), M2 (intermediate) and M3 (fine), where the grids M2 and M3 were generated by successive mesh refinements of M1. The grid spacing (δx) of the vertical lines is symmetric with respect to the expansion plane ($x = 0$). Far away from the expansion plane, for $|x| > 4.96h$, the grids have uniform δx. The grid spacing shrinks with a uniform contraction ratio $\xi_x = \delta x_{i+1}/\delta x_i = 0.96$, as we move closer to the expansion plane. The grid spacing (δy) of the horizontal lines is uniform, for $y < 0.675h$ and $y > 2.4h$. The contraction ratio of the grid spacing between adjacent horizontal lines, when moving closer to the plane of the channel wall ($y = h$), is $\xi_y^- = 0.93$ for $0.675 < y/h < 1$, and $\xi_y^+ = 0.95$ for $1 < y/h < 2.4$. The normalized minimum and maximum values of the grid spacing are reported in Table 2 for the three different meshes.

The time-step increment δt is dynamically adjusted in the in-house CFD code, with the adaptive time-stepping procedure described in [54]. In addition, δt was limited such that the maximum local Courant number does not exceed $C_{\max} = 0.25$. The residual tolerance for the non-linear successive substitution iterations (due to non-Newtonian constitutive models) was set to 10^{-6}. In practice, only a few number of iterations per time-step were needed. In *rheoTool*, the time-step increment was set according to the maximum Courant number $C_{\max} = 0.05$, and the vertical expansion wall was replaced by an outflow boundary condition, which is not expected to affect the flow field.

4.1. Numerical results for the Carreau fluid

This subsection reports the results of the extrudate swell predicted by the numerical simulations for the Carreau fluid. The extrudate swell is quantified by the *swell ratio*:

$$S_r = \frac{D_{\text{extr}}}{h},\qquad(37)$$

where D_{extr} is the half-width of the extrudate, after it has reached a uniform velocity profile, far from the die exit; see Fig. 5. We should note that the maximum half-width of the extrudate is frequently used in the literature to define S_r. However, our definition is more adequate to the

non-monotonic swell profiles that we obtained in some of the simulations, as will be shown later.

The extruded material experiences a modification of its velocity profile when exiting the extrusion die. The velocity profile varies from a fully-developed laminar flow, inside the channel, to a uniform rigid-body translation, far away from the channel exit. The rearrangement of the velocity profile and the relaxation of the normal stresses cause the extrudate swell [94]. The fully-developed laminar creeping flow of the Carreau fluids used approaches the power-law model, for which the velocity profile inside the channel depends on the power-law index n of the fluid as follows:

$$U(y) = U_0\left(1 - (y/h)^{\frac{n+1}{n}}\right),\ 0 \le y \le h,\qquad(38)$$

where U_0 is the maximum velocity at the channel centerline, which relates to the mean velocity $\overline{U}$ as:

$$U_0 = \left(\frac{2n+1}{n+1}\right)\overline{U}.\qquad(39)$$

The shear-thinning effect is controlled by the power-law index. If $n = 1$, the Newtonian fluid is recovered and the fully-developed flow has a parabolic velocity profile. As n decreases, the shear-thinning is enhanced, and the fully-developed velocity profile given in Eq. (38) becomes closer to a uniform plug flow. The limiting case where $n = 0$ corresponds to a solid-like plug flow with cohesive slip at the channel's wall, where only an infinitesimal boundary layer with an infinite shear rate would stick to the wall. Thus, shear-thinning reduces the extrudate swell, as it results in fully-developed channel flows closer to the uniform velocity profile, which require less velocity rearrangement at the die exit.

The numerical simulations of the generalized Newtonian fluid model did not present numerical difficulties. The simulations were stable and mesh-independent results were obtained for all the values of n tested. The numerical predictions of the extrudate swell with the three different schemes, are reported in Table 3, for the three meshes. The swell ratio as a function of the power-law index is also plotted in Fig. 6. As expected, the extrudate swell decreases as the power-law index is reduced. When $n < 0.3$, we obtain a swell ratio below one, meaning that the extrudate shrinks slightly. The influence of n in the swell ratio seems to be qualitatively similar to the inertia effects observed for Newtonian fluids elsewhere [95,96]. Furthermore, the extrudates display non-monotonic free-surface profiles for $0 < n < 0.5$, similarly to the regime of delayed extrudate swell observed for $6 \le Re \le 10$ [96]. In this range of n, the extrudate shrinks after the die exit, and then it swells until a constant S_r is attained.

The extrudate swell predictions from the schemes (I) and (II), based on the streamfunction/log-conformation formulation, converge toward the same values, on the finest mesh (M3). Nevertheless, the geometric CCU scheme (I) provided more accurate extrudate swell results than the algebraic HRIC scheme (II), on the coarse and intermediate meshes. The swell ratios predicted with the *rheoTool* solver (III) differ slightly from the two other schemes, especially when the power-law index is close to 1; however, the relative differences are below 1%, and decrease with mesh refinement. We also notice that on the coarser mesh resolution, the schemes (I) and (II) of the in-house solver over-estimate the swell ratio, while it is under-estimated in the scheme (III) implemented in *rheoTool*.

4.2. Numerical results for the Oldroyd-B fluid

The planar extrusion of the Oldroyd-B fluid was simulated for varying Weissenberg numbers, $Wi = \{0.5, 1, 1.5, 2, 2.5\}$, where the wall shear rate is used as the characteristic shear rate of the flow:

$$Wi = \lambda\dot{\gamma}_w = 3\lambda\overline{U}/h.\qquad(40)$$

A constant viscosity ratio $\beta = 1/9$ was used, similarly as in other

Table 2
Characteristics of the three grids used.

Mesh identifier:	M1	M2	M3
$\delta x/h = \delta y/h$ for $x = 0$ and $y = h$ (at the corner of the die exit)	0.0304	0.0152	0.0076
$\delta y/h$ for $y < 0.675h$ (near the symmetry line)	0.075	0.0375	0.01875
$\delta y/h$ for $y > 2.4h$ (far away from the symmetry line)	0.1	0.05	0.025
$\delta x/h$ for $|x| > 4.96h$ (far away from the expansion)	0.24	0.12	0.06
Number of control volumes	4340	17,360	69,440
Number of vertices	4527	17,733	70,185

Table 3
Extrudate swell ratio of the Carreau fluid as function of the power-law index n.

|	Numerical methodology								
	(I) Streamfunction/log-conformation + CCU			(II) Streamfunction/log-conformation + HRIC			(III) Rheotool		
n	M1	M2	M3	M1	M2	M3	M1	M2	M3
1	1.205	1.197	1.192	1.210	1.201	1.194	1.169	1.177	1.181
0.9	1.170	1.164	1.160	1.173	1.167	1.162	1.140	1.147	1.150
0.8	1.137	1.132	1.129	1.141	1.135	1.131	1.113	1.118	1.122
0.7	1.105	1.102	1.100	1.108	1.104	1.101	1.090	1.093	1.095
0.6	1.075	1.073	1.072	1.077	1.076	1.072	1.064	1.066	1.069
0.5	1.049	1.047	1.046	1.053	1.048	1.047	1.040	1.043	1.043
0.4	1.027	1.025	1.023	1.028	1.027	1.024	1.016	1.018	1.021
0.3	1.009	1.007	1.005	1.009	1.008	1.006	0.998	1.003	1.005
0.2	0.996	0.993	0.993	0.997	0.995	0.993	0.986	0.989	0.993
0.1	0.992	0.990	0.988	0.994	0.990	0.988	0.980	0.988	0.989
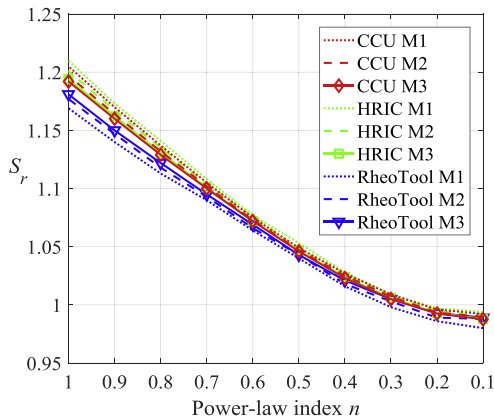
Fig. 6. Planar extrudate swell ratio of the Carreau fluid versus the power-law index n.

works, such that our numerical results could be compared with data[1] available in the literature [10,18,36,49]. In contrast with the Carreau fluid, the Oldroyd-B fluid has a constant shear viscosity. The fully-developed velocity profile of the Poiseuille creeping flow of the Oldroyd-B fluid is the same as for the Newtonian fluid, irrespectively of Wi and β. However, the viscoelastic Poiseuille flow does not only develop a shear stress τ_{xy} (like in purely viscous fluid flows), but also a viscoelastic normal stress component $\tau_{P,xx}$ in the direction of the flow. The viscoelastic normal stress component $\tau_{P,yy}$ in the transverse direction is zero for the fully-developed steady Poiseuille flow. However, there is a non-zero viscoelastic normal stress $\tau_{P,yy}$ in the die exit region, due to the flow rearrangement. According to Tanner's theory of extrudate swell [97], viscoelasticity contributes to an additional swell because of the relaxation of the elastic extra-stresses $\tau_{P,xy}$ and $\tau_{P,xx}$ into the extruded part. Indeed, the viscoelastic extra-stresses relax downstream of the die exit, as the extrudate is free from any external deformation constraint (i.e. the free surface of the extrudate is an open boundary condition). Tanner derived approximate solutions [97,98] of the additional swell due to viscoelasticity from the analytical stress profile inside the channel, which gives the following swell ratio for the planar extrusion of the Oldroyd-B model [94,98]:

$$S_r = 0.19 + \left(1 + \frac{S_w{}^2}{3}\right)^{1/4}, \tag{41}$$

where $S_w \equiv |N_1/2\tau_{xy}|_w$ is the "recoverable shear" at the die's wall and $N_1 = \tau_{P,xx} - \tau_{P,yy}$ is the first normal stress difference. Using the analytical expressions of the fully-developed stress profiles of the Oldroyd-B

model inside the channel and the definition of the Weissenberg number given in Eq. (40) yields:

$$S_w = (1 - \beta)\lambda\dot{\gamma}_w = (1 - \beta)Wi. \tag{42}$$

The term 0.19 in Eq. (41) is added to fit the value of the swell ratio of the Newtonian fluid (in planar extrusion), $S_r \approx 1.19$ when $S_w = 0$. According to the theory, increasing both Wi and $(1 - \beta)$ enhance the extrudate swell. However, Tanner's theory ignores the effect of the stress singularity at the die exit. Consequently, the solution of Tanner is only a valid approximation in the cases where the viscoelasticity of the extruded material has a low effect, i.e. when Wi is low or when β is close to 1.

Our numerical results of the swell ratio, simulated with the three different numerical schemes, on the three meshes with various degrees of refinement are presented in Table 4 and plotted in Fig. 7. Our results from the most refined mesh are compared in Fig. 7(a) with the other numerical data available in the literature, as well as the approximate solution given by Eq. (41). First, we can notice that there is a certain discrepancy between the different data available in the literature. Moreover, some of the data previously published was calculated on relatively coarse meshes, according to today's standard. For instance, the computational mesh of Crochet and Keunings [10] contained only 6 triangular finite elements (with biquadratic shape functions) in the half-width of the channel. Tomé et al. [36] used a uniform mesh with the grid spacing $\delta x/h = \delta y/h = 0.1$, which is approximately one order of magnitude higher than in our finest mesh. More recently, Habla et al. [49] simulated the planar extrudate swell for $Re = 0.5$, on a non-uniform grid with mesh refinement at the corner of the slit die, using the OpenFOAM® toolbox. The grid spacing was not provided in their publication, but the total number of control-volumes was only 4165, which is comparable to our coarsest mesh M1. Indeed, our results from mesh M1 are actually closer to the data previously published in [10,36,49] than our results from the finest mesh M3. The numerical results of Russo et al. [18] are not represented in Fig. 7(a) as they correspond to a different range of the Weissenberg number. They have only one data point that can actually be compared to our simulations: the swell ratio $S_r = 1.31$ for $Wi = 1.5$, which agrees relatively well with our results. Moreover, Russo et al. also provided a convergence analysis that shows the convergence of their results with the refinement of the spatial and temporal resolutions. Finally, we can see that Tanner's solution substantially deviates from the numerical calculations when $Wi > 1.5$. We also notice a small difference between Tanner's theory and the numerical simulations at $Wi = 0.5$, where the numerical simulations predict a decrease in the extrudate swell as compared to the Newtonian fluid, while Tanner's theory predicts a monotonic increase of the extrudate swell as Wi increases.

All our results calculated on the different meshes, with the three numerical schemes, are plotted in Fig. 7(b). We observe some

---

[1] The data from Ref. [18,36,49] have been adapted to the definition of the Weissenberg number adopted in our work.

Table 4
Extrudate swell ratio of the Oldroyd-B fluid. The values marked with $^{(*)}$ presented small persistent surface oscillations.

|	Numerical methodology								
	(I) Streamfunction/log-conformation + CCU			(II) Streamfunction/log-conformation + HRIC			(III) RheoTool		
Wi	M1	M2	M3	M1	M2	M3	M1	M2	M3
0	1.206	1.198	1.193	1.209	1.201	1.194	1.169	1.177	1.181
0.5	1.214	1.193	1.184	1.226	1.193	1.197	1.160	1.167	1.174
1	1.255	1.241	1.237	1.257	1.243	1.241	1.201	1.223	1.241
1.5	1.318	1.330	1.335	1.321	1.324	1.339	1.278	1.319	1.352
2	1.417	1.425	1.45 $^{(*)}$	1.418	1.425	1.46 $^{(*)}$	1.375	1.440	1.490
2.5	1.511	1.56 $^{(*)}$	1.59 $^{(*)}$	1.500	1.555	1.63 $^{(*)}$	1.494	1.576	1.639
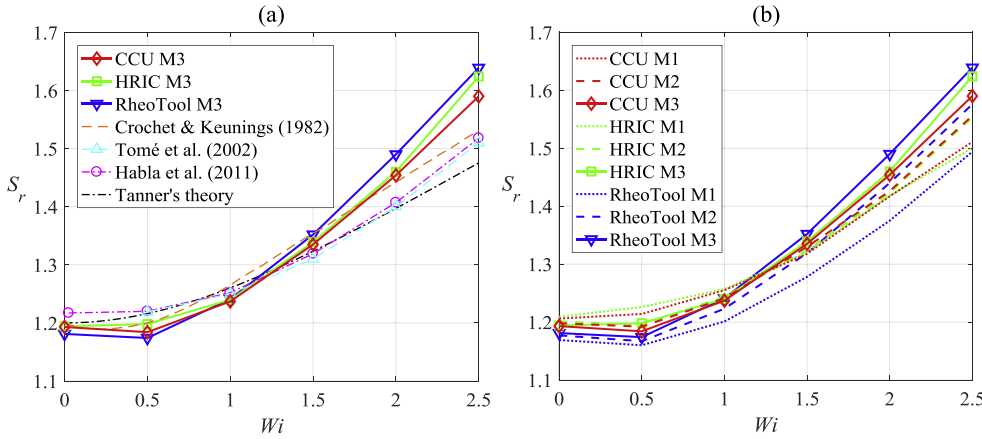
Fig. 7. Planar extrudate swell ratio of the Oldroyd-B fluid with $\beta = 1/9$: (a) Comparison of our results in the finest mesh (M3) with the data available in the literature; (b) Comparison of all our results obtained with different numerical schemes and mesh refinements.

discrepancy between the results obtained with the different numerical schemes for equal mesh, although the different schemes seem to be approaching a similar solution with mesh refinement. Our numerical solutions are not yet mesh independent, which means that some regions of the flow are still under-resolved and would require further mesh refinements (this is certainly the case in the die exit corner, where there is a singularity). Moreover, for $Wi > 1.5$, the calculations are prone to numerical instabilities in the position of the free surface, especially on the finest mesh. In some of the simulations, small ripples and self-sustained surface oscillations appeared at the free surface of the extrudate. These are believed to be numerical artifacts, and they will be discussed in Section 5.

4.3. Numerical results for the Giesekus fluid

The planar extrudate swell of the Giesekus fluid was simulated for two values of the mobility parameter, $\alpha = \{0.2, 0.5\}$, with the same viscosity ratio $\beta = 1/9$ as for the Oldroyd-B model, and for increasing Weissenberg numbers, $Wi = \{1, 2, 3, 4, 5, 6\}$. For all the numerical schemes, the extrusion simulations of the Giesekus fluid model were found more stable than those with the Oldroyd-B model. The free surface of the extrudate reached a steady position in all the simulations, except in one case where it developed persistent surface oscillations, when $Wi = 5$ and $\alpha = 0.2$, on mesh M3 with the CCU scheme.

The swell ratios are reported in Table 5 and plotted in Fig. 8, and are obtained from the final half-width of the extrudate far from the die exit, where the velocity has reached a uniform profile. We can see that the mobility parameter, which enhances the shear-thinning behavior, reduces the extrudate swell, presumably due to the same factors as in the Carreau fluid. As for the Oldroyd-B fluid, the minimum swell ratio is obtained for a certain Weissenberg number above zero, meaning that a small level of elasticity can reduce the extrudate swell as compared to the purely viscous case. The discrepancy between the simulations on the different meshes and with the different numerical schemes tends to

increase with the Weissenberg number. Moreover, some of the simulations with the HRIC algebraic scheme displayed small ripples on the free surface at the die exit, whose amplitudes are about the grid size. However, these ripples are damped and eventually become negligible as the material moves further downstream from the die exit. In contrast, the simulations with the CCU geometric scheme produces a smooth free surface of the extrudate, for most of the Wi numbers tested. Fig. 9 shows an example of the calculated free surfaces with the different schemes (PLIC reconstruction for the CCU scheme; 0.5-isoline of the liquid volume fraction for the HRIC and *rheoTool* MULES schemes), on mesh M3, for $Wi = 5$ and $\alpha = 0.5$.

In addition, the extrudates of the Giesekus fluid present a bulge at the die exit (non-monotonic free-surface profile), for $Wi \geq 2$. This bulge is due to a slight secondary shrinkage of the extrudate (i.e. the convergence of the streamlines) after its initial swell. We define the *extra-swell ES* as the relative difference between the half-width of bulge $D_{\max}$, and the half-width of the extrudate far from the die exit D_{extr}:

$$ES = \frac{D_{\max} - D_{\mathrm{extr}}}{D_{\mathrm{extr}}}. \tag{43}$$

The extra-swell quantifies the shrinkage of the extrudate after the initial swell. The values of the extra-swell for $Wi \geq 2$ are reported as bar charts in Fig. 10. Within the range $2 \leq Wi \leq 6$, the extra-swell seems to increase linearly with the Weissenberg number. Moreover, we did not observe significant differences in the extra-swell between the cases $\alpha = 0.2$ and $\alpha = 0.5$. The simulations with the CCU scheme and the *rheoTool* library present less discrepancy between the extra-swell calculated with the coarse and fine meshes than those with the HRIC scheme.

The small secondary shrinkage of the extrudate is attributed to relaxation of the negative tensile stress component $\tau_{P,yy}$. In contrast with the Oldroyd-B fluid, the Poiseuille flow for the Giesekus fluid develops a second normal stress difference inside the channel [99], $N_2 = \tau_{P,yy} = G(c_{22} - 1)$ in 2D. The extra-stress fields at the die exit are

Table 5

Extrudate swell ratio of the Giesekus fluid. The value marked with [*] presented small persistent surface oscillations, on the third decimal of the swell ratio.

	Numerical methodology								
	(I) Streamfunction/log-conformation + CCU			(II) Streamfunction/log-conformation + HRIC			(III) RheoTool		
Wi	M1	M2	M3	M1	M2	M3	M1	M2	M3
					$\alpha = 0.2$				
1	1.175	1.158	1.152	1.182	1.144	1.145	1.138	1.143	1.147
2	1.175	1.166	1.165	1.192	1.177	1.174	1.156	1.168	1.175
3	1.180	1.181	1.187	1.204	1.198	1.199	1.185	1.198	1.207
4	1.192	1.197	1.210	1.218	1.217	1.224	1.214	1.228	1.238
5	1.202	1.216	1.23 [*]	1.236	1.238	1.252	1.240	1.256	1.265
6	1.208	1.232	1.256	1.259	1.259	1.274	1.265	1.281	1.291
					$\alpha = 0.5$				
1	1.120	1.113	1.110	1.121	1.115	1.112	1.108	1.110	1.112
2	1.125	1.102	1.103	1.103	1.105	1.103	1.102	1.106	1.109
3	1.123	1.115	1.111	1.134	1.123	1.114	1.111	1.117	1.120
4	1.125	1.123	1.126	1.143	1.134	1.130	1.126	1.132	1.136
5	1.132	1.133	1.138	1.151	1.145	1.144	1.143	1.149	1.153
6	1.137	1.144	1.151	1.163	1.156	1.163	1.160	1.166	1.170

represented in Fig. 11, for the Oldroyd-B fluid ($Wi = 2$) and the Giesekus fluid ($Wi = 6$, $\alpha = 0.5$). First, we can see in Fig. 11 that the magnitude of the extra-stresses near the die corner are larger for the Oldroyd-B fluid than for the Giesekus fluid, although the former has a lower Weissenberg number. Indeed, the limitation of the steady planar extensional viscosity of the Giesekus fluid model (see Fig. 1) reduces the intensity of the stress singularity at the die exit corner. Secondly, we notice a difference in the $\tau_{P,yy}$ fields between the Oldroyd-B and the Giesekus fluid flows. The extrudate of the Giesekus fluid contains a surface layer with negative values of $\tau_{P,yy}$. The relaxation of the negative $\tau_{P,yy}$ component in this surface layer produces the secondary shrinkage of the extrudate after its initial swell. Finally, the extra-stress component $\tau_{P,xx} = G(c_{11} - 1)$ is one order of magnitude larger than the $\tau_{P,yy}$ component. Thus, in spite of the secondary shrinkage, the extrudate profile far from the die exit keeps a swell ratio above one, as shown in all the simulated test cases.

5. Discussion

The previous section has shown that the Eulerian simulations of purely viscous non-Newtonian fluids with the VOF method are robust, without numerical instabilities on the extrudate surface for all the

tested advection schemes. The use of shear rate-dependent viscosity models, as for instance the Carreau fluid model, and a simple rule of mixture by the weighted arithmetic mean of the viscosity in the interfacial control volumes reveals itself efficient. The integration of the viscous stresses over a control-volume Ω gives:

$$\frac{1}{V_\Omega} \int_\Omega \tau dV = \theta \widetilde{\tau}_1 + (1 - \theta)\widetilde{\tau}_2, \tag{44}$$

where $\widetilde{\tau}_1$ and $\widetilde{\tau}_2$ are the average stresses of the fluid phases 1 and 2 inside Ω, respectively. With a generalized Newtonian fluid model, the viscous stress in each phase is given by $\widetilde{\tau}_i = 2\eta_i(\widetilde{\dot{\gamma}_i})\widetilde{\mathbf{D}}_i$, where $\eta_i(\widetilde{\dot{\gamma}_i})$ is the effective viscosity, $\widetilde{\mathbf{D}}_i$ is the average rate-of-deformation tensor inside the liquid phase i and $\widetilde{\dot{\gamma}_i} = \sqrt{2\{\widetilde{\mathbf{D}}_i : \widetilde{\mathbf{D}}_i\}}$, with $i = 1, 2$. Furthermore, the use of finite differences to compute the stress integral yields the approximation

$$2\theta\eta_1(\widetilde{\dot{\gamma}_1})\widetilde{\mathbf{D}}_1 + 2(1 - \theta)\eta_2(\widetilde{\dot{\gamma}_2})\widetilde{\mathbf{D}}_2 \approx 2[\theta\eta_1(\dot{\gamma}_{\text{mix}}) + (1 - \theta)\eta_2(\dot{\gamma}_{\text{mix}})]\mathbf{D}_{\text{mix}}, \tag{45}$$

where $\mathbf{D}_{\text{mix}}$ is an estimate of the average rate-of-deformation tensor of the fluids' mixture and $\dot{\gamma}_{\text{mix}} = \sqrt{2\{\mathbf{D}_{\text{mix}} : \mathbf{D}_{\text{mix}}\}}$ is the average shear rate inside the control volume. This approximation results in additional discretization errors in the velocities at the interfacial cells; however,
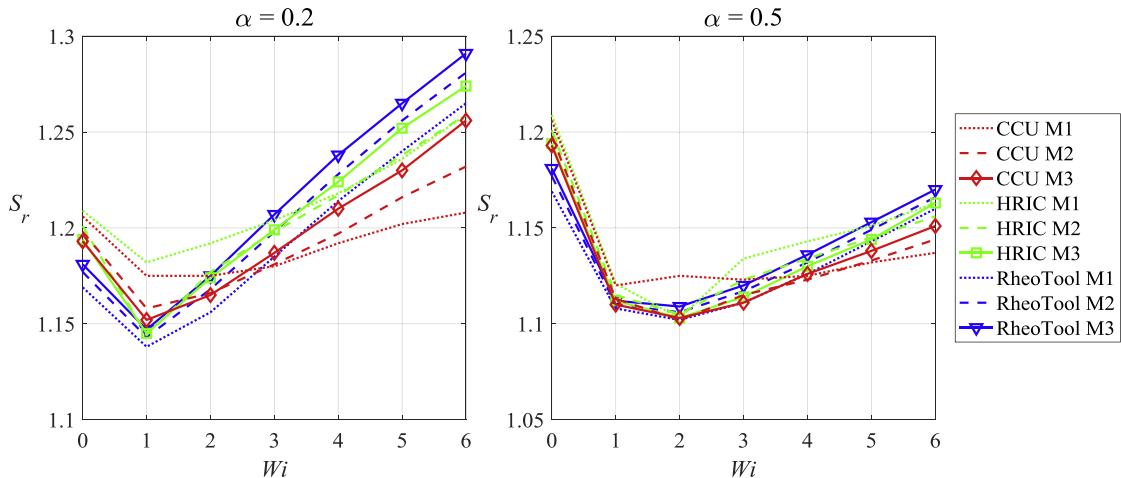

Fig. 8. Planar extrudate swell ratio of the Giesekus fluid model with a viscosity ratio $\beta = 1/9$, for Weissenberg numbers within the range $Wi \in [0, 6]$, and for the mobility factors $\alpha = 0.2$ and $\alpha = 0.5$. Predictions of the different numerical schemes, for various mesh refinements. (The lines are only a guide to the eye.).
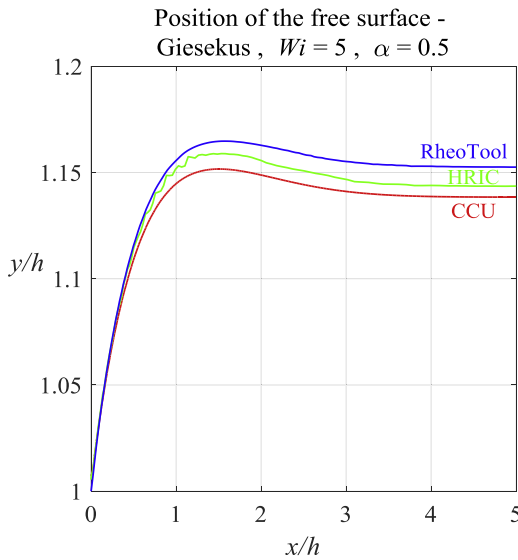
Fig. 9. Free-surface location of the extrudate for the Giesekus fluid model ($Wi = 5$ and $\alpha = 0.5$), calculated on mesh M3 with the CCU scheme (PLIC reconstruction), the HRIC scheme and the *rheoTool* library (0.5-isoline of the liquid volume fraction).

the error is bounded, as $\min(\widetilde{\dot{\gamma}}_1, \widetilde{\dot{\gamma}}_2) \leq \dot{\gamma}_{\mathrm{mix}} \leq \max(\widetilde{\dot{\gamma}}_1, \widetilde{\dot{\gamma}}_2)$. Thus, the numerical errors due to the finite-difference approximations within the Eulerian framework of the purely viscous stresses of the mixture in the interfacial cells converge to zero when the mesh is refined.

The situation is different for the numerical integration of the viscoelastic extra-stresses, as there are no upper bounds for the discretization errors of τ_P. In contrast to purely viscous stresses, the viscoelastic extra-stresses are not expressed in terms of the rate-of-deformation tensor with an algebraic relation, but using a partial differential equation. Our numerical experiments show that it is difficult to obtain stable and mesh-independent solutions of the extrusion of viscoelastic fluids, when the Weissenberg number is above one. The presence of a stress singularity at the wall exit corner does not

guarantee that the numerical results will converge to a mesh-independent solution with additional mesh refinements. Indeed, as the mesh is refined, discrete solutions are computed closer to the location of the stress singularity, involving larger extra-stress gradients in the calculations. In practice, we see that the mesh refinements promote free-surface instabilities of the Oldroyd-B fluid. Moreover, the results are also affected by the choice of the VOF method (i.e. geometric versus algebraic advection schemes).

We observed two types of instabilities lying on the extrudate surface. First, for the HRIC scheme (and the *rheoTool* MULES scheme to a less extent), the free surface was prone to the *ripple numerical artifact*, illustrated in Fig. 9, which appears at the location where the extrudate swells or shrinks. The ripples are eventually damped out downstream and do not affect the steady swell ratio of the extrudate. The ripple numerical artifacts come from the approximation of the free-surface position with the 0.5-isoline of the liquid volume fraction, within the algebraic VOF methods. Furthermore, the location of the free surface loses precision during the simulation, as the algebraic VOF methods tend to smear the transition of the liquid volume fractions between the fully-filled and empty cells over a few control volumes. In contrast, the geometric VOF methods preserve sharp interfaces, thanks to the PLIC reconstruction. In addition, the second-order accurate ELVIRA interface reconstruction method smoothens the second derivative of the interface [84]. Thus, the CCU scheme has a better resolution than for instance the HRIC scheme, and it is not subjected to the ripples numerical artifacts.

The second type of surface instabilities consists in *self-sustained surface oscillations* that occur when the Weissenberg number exceeds a critical value. This type of instabilities has only been observed in the simulations with the in-house CFD code, i.e. the schemes (I) and (II). Examples of self-sustained surface oscillations are represented in Fig. 12. The surface oscillation is initiated at the contact point between the free surface and the expansion wall, in the vicinity of the stress singularity. Then, the surface oscillation is advected along the extrudate by the surface-tracking algorithm. In contrast to the ripple numerical artifacts, these surface oscillations are not attributed to flaws in the surface-tracking methods, as they equally occur with the CCU geometric scheme and the HRIC algebraic scheme. Moreover, the amplitude of these surface oscillations are larger than the grid resolution, and
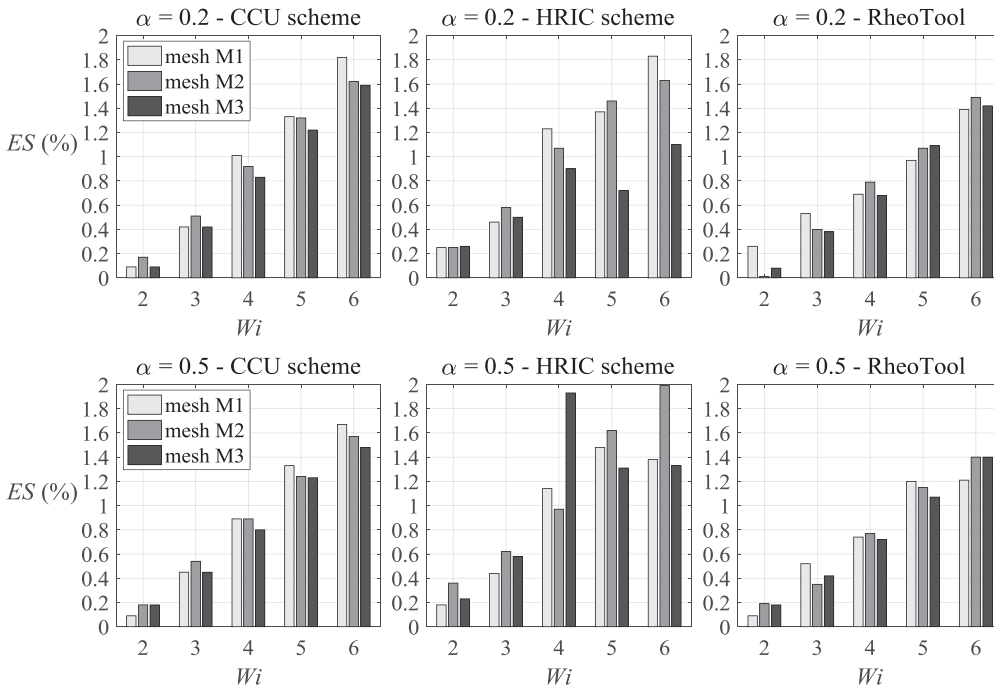

Fig. 10. Percentage of the extra-swell *ES* for the extrusion of the Giesekus fluid with $\alpha = 0.2$ (top) and $\alpha = 0.5$ (bottom). Comparison of the three numerical schemes (CCU; HRIC; *rheoTool*) on the three meshes M1, M2 and M3, over the range $Wi \in [2, 6]$.
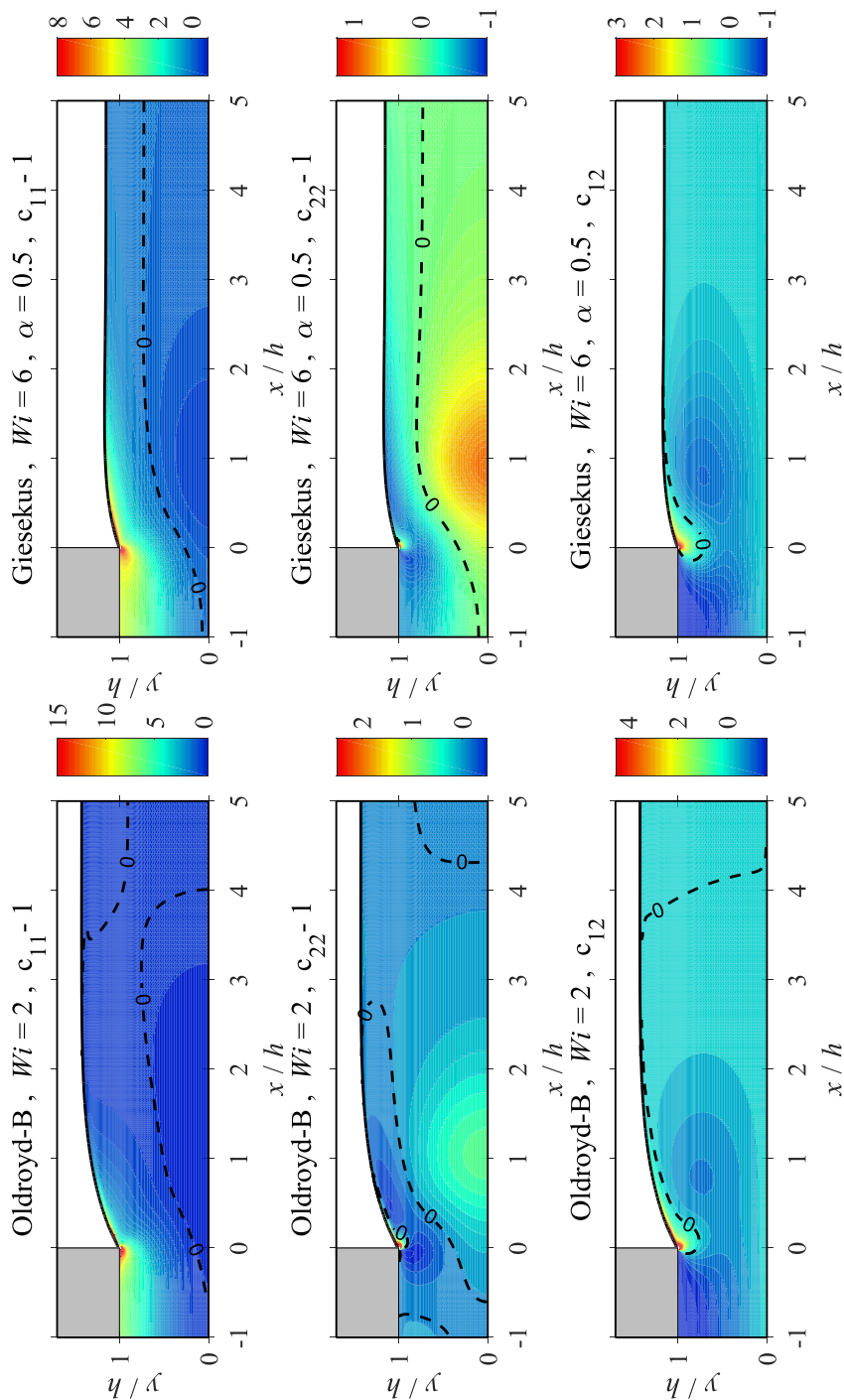
Fig. 11. Contour maps of the conformation tensor components at the die exit, for the Oldroyd-B fluid with $Wi = 2$ (left), and for the Giesekus fluid with $\alpha = 0.5$ and $Wi = 6$ (right), in mesh M3, using the CCU scheme. The dashed lines represent the zero isolines that separate the positive and negative stress regions. (The large extra-stresses at the die corner singularity have been removed.).
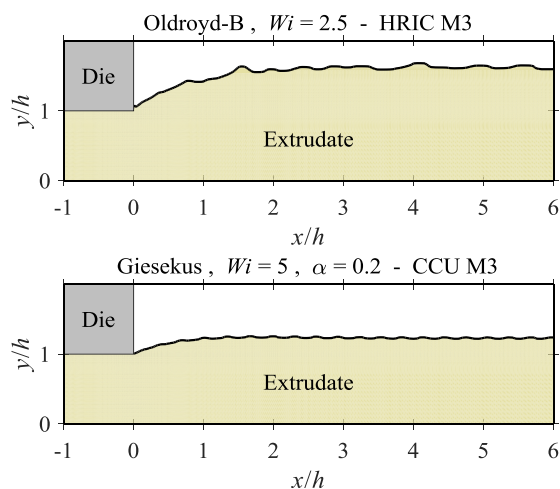
Fig. 12. Examples of the self-sustained surface oscillation numerical artifact, for the Oldroyd-B and the Giesekus fluid models, calculated on mesh M3, with the CCU and the HRIC schemes.

the mesh refinement promotes the onset of the surface oscillations. It is interesting to note that these self-sustained instabilities present spatial and temporal regularity. Similar surface instabilities have been reported in the recent extrusion simulations of Kwon [100], who also employed the Eulerian flow description. His simulations used the level-set method and a variant of the Leonov constitutive model [101], reformulated with the log-conformation representation [102]. The surface oscillations in the numerical simulations of Kwon [100] were attributed to the *sharkskin* and the *gross melt fracture* extrusion defects.

The self-sustained surface oscillations present in some of our simulations (see Fig. 12) visually resemble the sharkskin extrusion defect. Cogswell [103] proposed a sharkskin mechanism where the surface defects arise from the tearing and cracking of the material at the surface of the extrudate, just downstream of the die exit, when the skin layer is subjected to large tensile stresses due to the change of boundary condition. The experimental investigations conducted in [104,105] validate this hypothesis. However, beyond the fact that both in the experiments and in the numerical simulations the surface oscillations occur with the presence of large tensile stresses at the die exit, we do not have any evidence that the surface oscillations of our simulations represent a physical phenomenon. Thus, we prefer to interpret them as a numerical artifact due to the approximations of the two-phase flow with the Eulerian surface-capturing approach. The fact that we predominantly observed this numerical artifact with the Oldroyd-B model (and in only one simulation with the Giesekus model) when the Weissenberg number is above one suggests that it might be related to the stress singularity at the die corner. We hypothesize that the numerical calculation of the extra-stresses in the vicinity of the channel exit is prone to large numerical errors because of the stress singularity, which also affect the velocity field and the position of the free surface. In return, the erratic displacement of the free surface affects the amount of extra-stresses inside the interfacial control volume, as the liquid volume fraction enters the formula (28) of the apparent elastic modulus of the mixture.

Looking into more detail at the Eulerian surface-capturing representation of the flow, we see that the finite-difference scheme produces inaccurate estimations of the velocity gradient and the divergence of the extra-stress tensor inside the interfacial control volumes. The finite-difference scheme evaluates the average velocity gradient of the mixture of the two fluid phases inside the cell, which is then used in the upper-convected time derivative of the differential viscoelastic constitutive model and in its transformation with the log-conformation representation. However, as the air phase has a much lower apparent

viscosity than the viscoelastic fluid ($\eta_{air}/\eta \approx 10^{-5}$), the average velocity gradient of the mixture is generally much larger than the velocity gradient inside the viscoelastic phase. Thus, the constitutive solver calculates the extra-stress based on a wrong evaluation of the velocity gradient inside the viscoelastic fluids. The resulting numerical errors in the extra-stresses have an impact on the source terms of the momentum equation. Furthermore, the calculation of the divergence of the extra-stress tensor in the interfacial control volumes also introduces numerical approximations. The finite-difference scheme of the divergence operator must avoid two pitfalls, in particular. First, the empty cells neighboring an interfacial cell must not "feel" the extra-stress of the viscoelastic fluid inside the nearby cells. Indeed, any extra-stress source term in an empty cell may produce an enormous vorticity in this cell (as the air has a very low viscosity and density) that would wrongly deform the interface. Secondly, it is important that the momentum equations relative to the faces of interfacial cells receive a correct amount of extra-stress in their source terms. Otherwise, an incorrect value of the extra-stress at the free surface of the extrudate would produce a stress imbalance, resulting in erroneous extrudate swell. For instance, in one of our preliminary tests, the extrusion simulations with a numerical scheme that ignored the extra-stress gradient at the faces of the interfacial cells produced unlimited swell. We took a special care to implement an acceptable numerical scheme that avoids these two issues in our in-house code. In the present finite-difference scheme, the calculation of the extra-stress divergence uses a linear interpolation of the cell-averaged values of the shear component of the extra-stress tensor from the center of the cells to their vertices. This linear interpolation produces a smoothing of the shear extra-stress at the cell's vertices, which, we believe, can induce unphysical accelerations or decelerations in the neighboring cells to the interface, as there is a discontinuity in the extra-stress. Despite our efforts, we did not succeed to eliminate completely the self-sustained surface instability due to the feedback effects of the numerical errors between the extra-stresses, the velocity and the position of the free surface.

In contrast, the simulations in *rheoTool* were more stable and do not suffered from self-sustained instabilities. Several reasons could explain this different behavior, but it is likely that the several stabilization mechanisms included in *rheoTool* contributed to a big extent. Among them, we can highlight the pressure smoothing by the Rhie-Chow interpolation of fluxes and the stress-velocity coupling algorithm [67].

The discrepancy between the results of the different numerical schemes, as well as the occurrence of numerical artifacts, highlight the difficulties to simulate free-surface viscoelastic flows with an Eulerian surface-capturing method, when there is a stress singularity near the interface. The numerical simulations of the Oldroyd-B model are important from a computational point of view, as it is the basis for most non-linear differential viscoelastic models. However, many of the numerical issues that are encountered above a critical Weissenberg number are amplified by the inability of the Oldroyd-B model to correctly describe strong extensional flows compared with other models that predict shear-thinning, such as the Giesekus model (see Fig. 1). Indeed, we obtained stable extrusion simulations of the Giesekus fluid for larger *Wi* than for the Oldroyd-B model. Nevertheless, the Giesekus model is derived from a relatively simple idealized molecular model, as compared to the complexity of real polymeric liquids. More recent constitutive models based on molecular theories that take into account the reptation motion of the macromolecules, the chain retraction and the convective constraint release [106–110] provide a more accurate description of rheometric flows of monodisperse linear polymers and branched polymers. Moreover, the polymeric flow inside the die can be subjected to partial wall slip, involving chain detachment (adhesive failure), chain disentanglement (cohesive failure), an hysteretic transition between the slip regimes, and potential stick-slip instabilities [111], which should also be taken into account in the models to predict accurately the extrusion flow at large deformation rates.

6. Conclusions

We have presented an original numerical algorithm to solve incompressible non-Newtonian free-surface flows, based on the coupling of the streamfunction flow formulation with a geometric VOF surface-capturing method. The flow solver was further coupled with a viscoelastic constitutive stress solver. The log-conformation representation was applied to the differential viscoelastic models, to reformulate the constitutive equations in terms of the matrix-logarithm of the conformation tensor. The proposed method has the following advantages:

- The continuity characteristic of incompressible flows is automatically satisfied with the streamfunction flow solver, which calculates the vector potentials of the solenoidal velocity field.
- The positive-definiteness of the conformation tensor is guaranteed by the log-conformation representation, which prevents the occurrence of the high Weissenberg number instability.
- The liquid volume is conserved and kept physically-bounded by the geometric CCU advection scheme, which provides a sharp representation of the free surface.
- The removal of the pressure variable with the streamfunction flow formulation reduces the number of unknowns and facilitates the convergence of segregated multi-physics solvers. Moreover, the pressure-free immiscible two-phase flow solver is able to undergo large ratios of densities and viscosities, in the absence of surface-tension effects.

The proposed method was applied to the simulation of the extrudate swell problem, for pseudoplastic fluids (Carreau model), quasi-linear viscoelastic fluids (Oldroyd-B model) and non-linear viscoelastic fluids (Giesekus model). The extrusion test cases were also solved with an algebraic VOF method (HRIC scheme), as an alternative to the geometric VOF method. Finally, the calculations were verified with the *rheoTool* library, which uses a semi-implicit velocity-pressure coupling method and an algebraic VOF scheme for interface advection.

The numerical simulations of the pseudoplastic fluids with the Carreau model provided stable and mesh-independent results, also revealing a good matching between the different numerical schemes. The numerical results confirm that shear-thinning reduces the extrudate swell, as the flow requires less rearrangement at the die exit.

The results of the extrudate swell for the Oldroyd-B model are in qualitative agreement with the data available in the literature. However, the calculations are very sensitive to mesh refinement and to the choices of the numerical schemes. We also observed some discrepancies between the results available in the literature, although this problem has received significant attention. Above a critical Weissenberg number, the simulations of the Oldroyd-B fluid were prone to surface instabilities, including small ripples due to the algebraic VOF schemes, and self-sustained surface oscillations which are attributed to the two-phase Eulerian formulation that erroneously averages the velocity gradient and the extra-stress divergence around the interface. These numerical artifacts illustrate the difficulty to simulate free-surface viscoelastic flows under an Eulerian description. Moreover, the numerical issues are likely related to the presence of a stress singularity at the corner of the die exit, and to the deficiencies of the Oldroyd-B fluid in strong extensional flows.

In contrast, the simulations with the Giesekus model are less prone to surface instabilities. Stable extrusion simulations with the Giesekus fluid were achieved at larger Weissenberg numbers than with the Oldroyd-B fluid. The quadratic term in the Giesekus constitutive model (when $\alpha \neq 0$) limits the steady extensional viscosity of the fluid, which lowers the magnitude of the normal stresses on the walls and at the die exit. The shear-thinning behavior of the Giesekus fluid also reduces the extrudate swell as compared to the Oldroyd-B fluid. In addition, we found out that after the initial swell, the extrudate slightly shrinks before it reaches its uniform steady flow profile. The relative difference between the maximum swell ratio and the steady-state swell ratio, which we refer to as the extra-swell, increases quasi-linearly with the Weissenberg number, within the range $2 \leq Wi \leq 6$. The proposed method has only been tested in two-dimensional test cases, and a future work will address the extension of this methodology to three-dimensional calculations.

Acknowldgments

References

[1] H.W. Jung, J.C. Hyun, Instabilities in extensional deformation polymer processing, Rheol. Rev. (2006) 131–164.

[2] Y. Demay, J.F. Agassant, An overview of molten polymer drawing instabilities, Int. Polym. Proc. 29 (2014) 128–139.

[3] J.F. Agassant, D.R. Arda, C. Combeaud, A. Merten, H. Müenstedt, M.R. Mackley, L. Robert, B. Vergnes, Polymer processing extrusion instabilities and methods for their elimination or minimisation, Int. Polym. Proc. 21 (2006) 239–255.

[4] B. Meulenbroek, C. Storm, V. Bertola, C. Wagner, D. Bonn, W. van Saarloos, Intrinsic route to melt fracture in polymer extrusion: a weakly nonlinear subcritical instability of viscoelastic Poiseuille flow, Phys. Rev. Lett. 90 (2003) 024502.

[5] N. Lebaal, F. Schmidt, S. Puissant, Design and optimization of three-dimensional extrusion dies, using constraint optimization algorithm, Finite Elem. Anal. Des. 45 (2009) 333–340.

[6] S. Elgeti, M. Probst, C. Windeck, M. Behr, W. Michaeli, C. Hopmann, Numerical shape optimization as an approach to extrusion die design, Finite Elem. Anal. Des. 61 (2012) 35–43.

[7] L. Pauli, M. Behr, S. Elgeti, Towards shape optimization of profile extrusion dies with respect to homogeneous die swell, J. Non Newton. Fluid Mech. 200 (2013) 79–87.

[8] R.B. Bird, R.C. Armstrong, O. Hassager, Dynamics of polymeric liquids, Vol 1: Fluid mechanics, second ed, Wiley-Interscience Publication, 1987.

[9] M.J. Crochet, R. Keunings, Die swell of a Maxwell fluid: numerical prediction, J. Non Newton. Fluid Mech. 7 (1980) 199–212.

[10] M.J. Crochet, R. Keunings, Finite element analysis of die swell of a highly elastic fluid, J. Non Newton. Fluid Mech. 10 (1982) 339–356.

[11] O. Wambersie, M.J. Crochet, Transient finite element method for calculating steady state three-dimensional free surfaces, Int. J. Numer. Meth. Fluids 14 (1992) 343–360.

[12] E. Mitsoulis, Three-dimensional non-Newtonian computations of extrudate swell with the finite element method, Comput. Methods Appl. Mech. Eng. 180 (1999) 333–344.

[13] E. Mitsoulis, Annular extrudate swell of pseudoplastic and viscoplastic fluids, J. Non Newton. Fluid Mech. 141 (2007) 138–147.

[14] M.B. Bush, J.F. Milthorpe, R.I. Tanner, Finite element and boundary element methods for extrusion computations, J. Non Newton. Fluid Mech. 16 (1984) 37–51.

[15] J.R. Clermont, M. Normandin, Numerical simulation of extrudate swell for Oldroyd-B fluids using the stream-tube analysis and a streamline approximation, J. Non Newton. Fluid Mech. 50 (1993) 193–215.

[16] S. Tanoue, T. Kajiwara, Y. Iemoto, K. Funatsu, High Weissenberg number simulation of an annular extrudate swell using the differential type constitutive equation, Polym. Eng. Sci. 38 (1998) 409–419.

[17] G. Karapetsas, J. Tsamopoulos, Steady extrusion of viscoelastic materials from an annular die, J. Non Newton. Fluid Mech. 154 (2008) 136–152.

[18] G. Russo, T.N. Phillips, Spectral element predictions of die-swell for Oldroyd-B fluids, Comput. Fluids 43 (2011) 107–118.

[19] G. Russo, T.N. Phillips, Numerical prediction of extrudate swell of branched polymer melts, Rheol. Acta 49 (2010) 657–676.

[20] M. Normandin, J.R. Clermont, J. Guillet, C. Raveyre, Three-dimensional extrudate swell experimental and numerical study of a polyethylene melt obeying a memory-integral equation, J. Non Newton. Fluid Mech. 87 (1999) 1–25.

[21] H.K. Rasmussen, O. Hassager, Three-dimensional simulations of viscoelastic instability in polymeric filaments, J. Non Newton. Fluid Mech. 82 (1999) 189–202.

[22] J.M.R. Marin, H.K. Rasmussen, Lagrangian finite–element method for the simulation of K-BKZ fluids with third order accuracy, J. Non Newton. Fluid Mech. 156 (2009) 177–188.

[23] J. Étienne, E.J. Hinch, J. Li, A Lagrangian–Eulerian approach for the numerical simulation of free-surface flow of a viscoelastic material, J. Non Newton. Fluid Mech. 136 (2006) 157–166.

[24] K.S. Sujatha, H. Matallah, M.J. Banaai, M.F. Webster, Computational predictions for viscoelastic filament stretching flows: ALE methods and free-surface techniques

(CM and VOF), J. Non Newton. Fluid Mech. 137 (2006) 81–102.

[25] V. Ganvir, A. Lele, R. Thaokar, B.P. Gautham, Prediction of extrudate swell in polymer melt extrusion using an Arbitrary Lagrangian Eulerian (ALE) based finite element method, J. Non Newton. Fluid Mech. 156 (2009) 21–28.

[26] Y. Cao, X.G. Ren, X.W. Guo, M. Wang, Q. Wang, X.H. Xu, X.J. Yang, A new method to simulate free surface flows for viscoelastic fluid, Adv. Mater. Sci. Eng. (2015) 159831.

[27] J. Fang, R.G. Owens, L. Tacher, A. Parriaux, A numerical study of the SPH method for simulating transient viscoelastic free surface flows, J. Non Newton. Fluid Mech. 139 (2006) 68–84.

[28] A. Rafiee, M.T. Manzari, M. Hosseini, An incompressible SPH method for simulation of unsteady viscoelastic free-surface flows, Int. J. Non Linear Mech. 42 (2007) 1210–1223.

[29] X. Xu, J. Ouyang, T. Jiang, Q Li, Numerical simulation of 3D-unsteady viscoelastic free surface flows by improved smoothed particle hydrodynamics method, J. Non Newton. Fluid Mech. 177 (2012) 109–120.

[30] C. Chung, M.A. Hulsen, J.M. Kim, K.H. Ahn, S.J. Lee, Numerical study on the effect of viscoelasticity on drop deformation in simple shear and 5:1:5 planar contraction/expansion microchannel, J. Non Newton. Fluid Mech. 155 (2008) 80–93.

[31] D. Izbassarov, M. Muradoglu, A front-tracking method for computational modeling of viscoelastic two-phase flow systems, J. Non Newton. Fluid Mech. 223 (2015) 122–140.

[32] M.F. Tomé, J.A. Cuminato, N. Mangiavacchi, S. McKee, GENSMAC3D: a numerical method for solving unsteady three-dimensional free surface flows, Int. J. Numer. Meth. Fluids 37 (2001) 747–796.

[33] S. McKee, M.F. Tomé, V.G. Ferreira, J.A. Cuminato, A. Castelo, F.S. Sousa, N. Mangiavacchi, The MAC method, Comput. Fluids 37 (2008) 907–930.

[34] M.F. Tomé, B. Duffy, S. McKee, A numerical technique for solving unsteady non-Newtonian free surface flows, J. Non Newton. Fluid Mech. 62 (1996) 9–34.

[35] M.F. Tomé, L. Grossi, A. Castelo, J.A. Cuminato, N. Mangiavacchi, V.G. Ferreira, F.S. De Sousa, S. McKee, A numerical method for solving three-dimensional generalized Newtonian free surface flows, J. Non Newton. Fluid Mech. 123 (2004) 85–103.

[36] M.F. Tomé, N. Mangiavacchi, J.A. Cuminato, A. Castelo, S. McKee, A finite difference technique for simulating unsteady viscoelastic free surface flows, J. Non Newton. Fluid Mech. 106 (2002) 61–106.

[37] M.F. Tomé, A. Castelo, V.G. Ferreira, S. McKee, A finite difference technique for solving the Oldroyd-B model for 3D-unsteady free surface flows, J. Non Newton. Fluid Mech. 154 (2008) 179–206.

[38] G. Mompean, L. Thais, M.F. Tomé, A. Castelo, Numerical prediction of three-dimensional time-dependent viscoelastic extrudate swell using differential and algebraic models, Comput. Fluids 44 (2011) 68–78.

[39] M.F. Tomé, G.S. Paulo, F.T. Pinho, M.A. Alves, Numerical solution of the PTT constitutive equation for unsteady three-dimensional free surface flows, J. Non Newton. Fluid Mech. 165 (2010) 247–262.

[40] R.A. Figueiredo, C.M. Oishi, J.A. Cuminato, M.A. Alves, Three-dimensional transient complex free surface flows: Numerical simulation of XPP fluid, J. Non Newton. Fluid Mech. 195 (2013) 88–98.

[41] M.F. Tomé, J. Bertoco, C.M. Oishi, M.S.B. Araujo, D. Cruz, F.T. Pinho, M. Vynnycky, A finite difference technique for solving a time strain separable K-BKZ constitutive equation for two-dimensional moving free surface flows, J. Comput. Phys. 311 (2016) 114–141.

[42] J.A. Sethian, P. Smereka, Level set methods for fluid interfaces, Annu. Rev. Fluid Mech. 35 (2003) 341–372.

[43] J.-D. Yu, S. Sakai, J.A. Sethian, Two-phase viscoelastic jetting, J. Comput. Phys. 220 (2007) 568–585.

[44] E. Castillo, J. Baiges, R. Codina, Approximation of the two-fluid flow problem for viscoelastic fluids using the level set method and pressure enriched finite element shape functions, J. Non Newton. Fluid Mech. 225 (2015) 37–53.

[45] W.J. Rider, D.B. Kothe, Reconstructing volume tracking, J. Comput. Phys. 141 (1998) 112–152.

[46] R.A. Figueiredo, C.M. Oishi, A.M. Afonso, I.V.M. Tasso, J.A. Cuminato, A two-phase solver for complex fluids: Studies of the Weissenberg effect, Int. J. Multiphase Flow 84 (2016) 98–115.

[47] A. Bonito, M. Picasso, M. Laso, Numerical simulation of 3D viscoelastic flows with free surfaces, J. Comput. Phys. 215 (2006) 691–716.

[48] J.L. Favero, A.R. Secchi, N.S.M. Cardozo, H. Jasak, Viscoelastic fluid analysis in internal and in free surface flows using the software OpenFOAM, Comput. Chem. Eng. 34 (2010) 1984–1993.

[49] F. Habla, H. Marschall, O. Hinrichsen, L. Dietsche, H. Jasak, J.L. Favero, Numerical simulation of viscoelastic two-phase flows using openFOAM®, Chem. Eng. Sci. 66 (2011) 5487–5496.

[50] P.A. Stewart, N. Lay, M. Sussman, M. Ohta, An improved sharp interface method for viscoelastic and viscous two-phase flows, J. Sci. Comput. 35 (2008) 43–61.

[51] R. Scardovelli, S. Zaleski, Direct numerical simulation of free-surface and interfacial flow, Annu. Rev. Fluid Mech. 31 (1999) 567–603.

[52] J.-R. Clermont, Analysis of incompressible three-dimensional flows using the concept of stream tubes in relation with a transformation of the physical domain, Rheol. Acta 27 (1988) 357–362.

[53] J.-R. Clermont, D. Grecov, A theoretical analysis of unsteady incompressible flows for time-dependent constitutive equations based on domain transformations, Int. J. Non Linear Mech. 44 (2009) 709–715.

[54] R. Comminal, J. Spangenberg, J.H. Hattel, Robust simulations of viscoelastic flows at high Weissenberg numbers with the streamfunction/log-conformation formulation, J. Non Newton. Fluid Mech. 223 (2015) 37–61.

[55] R. Comminal, J.H. Hattel, M.A. Alves, J. Spangenberg, Vortex behavior of the Oldroyd-B fluid in the 4-1 planar contraction simulated with the streamfunction–log-conformation formulation, J. Non Newton. Fluid Mech. 237 (2016) 1–15.

[56] R. Kupferman, A central-difference scheme for a pure stream function formulation of incompressible viscous flow, SIAM J. Sci. Comput. 23 (2001) 1–18.

[57] V.I. Bubnovich, C.E. Rosas, N.O. Moraga, A stream function implicit finite difference scheme for 2D incompressible flows of Newtonian fluids, Int. J. Numer. Meth. Eng. 53 (2002) 2163–2184.

[58] M. Ben-Artzi, J.-P. Croisille, D. Fishelov, S. Trachtenberg, A pure-compact scheme for the streamfunction formulation of Navier–Stokes equations, J. Comput. Phys. 205 (2005) 640–664.

[59] M.H. Kobayashi, J.M.C. Pereira, A computational stream function method for two-dimensional incompressible viscous flows, Int. J. Numer. Meth. Eng. 62 (2005) 1950–1981.

[60] Z.F. Tian, P.X. Yu, An efficient compact difference scheme for solving the streamfunction formulation of the incompressible Navier–Stokes equations, J. Comput. Phys. 230 (2011) 6404–6419.

[61] R. Fattal, R. Kupferman, Constitutive laws for the matrix-logarithm of the conformation tensor, J. Non Newton. Fluid Mech. 123 (2004) 281–285.

[62] R. Fattal, R. Kupferman, Time-dependent simulation of viscoelastic flows at high Weissenberg number using the log-conformation representation, J. Non Newton. Fluid Mech. 126 (2005) 23–37.

[63] R. Comminal, J. Spangenberg, J.H. Hattel, A two-phase flow solver for incompressible viscous fluids, using a pure streamfunction formulation and the volume of fluid technique, Defect Diffus. Forum 348 (2014) 9–19.

[64] R. Comminal, J. Spangenberg, J.H. Hattel, Cellwise conservative unsplit advection for the volume of fluid method, J. Comput. Phys. 283 (2015) 582–608.

[65] S. Muzaferijam, M. Peric, P. Sames, T. Schellin, A two-fluid Navier–Stokes solver to simulate water entry, Proceedings of the 22nd Symposium on Naval Hydrodynamics, 1999, pp. 277–289.

[66] F. Pimenta, M.A. Alves, RheoTool User Guide, ver. 1.0, (2017) March 31. Available online at https://github.com/fppimenta/rheoTool.

[67] F. Pimenta, M.A. Alves, Stabilization of an open-source finite-volume solver for viscoelastic fluid flows, J. Non Newton. Fluid Mech. 239 (2017) 85–104.

[68] H. Jasak, A. Jemcov, Z. Tukovic, OpenFOAM: a C++ library for complex physics simulations, International Workshop on Coupled Methods in Numerical Dynamics, IUC Dubrovnik, Croatia, 2007, pp. 1–20.

[69] J.G. Oldroyd, On the formulation of rheological equations of state, Proc. R. Soc. Lond. A Math. Phys. Sci. 200 (1950) 523–541.

[70] L.J. Amoreira, P.J Oliveira, Comparison of different formulations for the numerical calculation of unsteady incompressible viscoelastic fluid flow, Adv. Appl. Math. Mech. 4 (2010) 483–502.

[71] H.A. Kramers, The behavior of macromolecules in inhomogeneous flow, J. Chem. Phys. 14 (1946) 415–424.

[72] H. Giesekus, A unified approach to a variety of constitutive models for polymer fluids based on the concept of configuration-dependent molecular mobility, Rheol. Acta 21 (1982) 366–375.

[73] R.B. Bird, J.M. Wiest, Anisotropic effects in dumbbell kinetic theory, J. Rheol. 29 (1985) 519–532.

[74] H. Giesekus, A simple constitutive equation for polymer fluids based on the concept of deformation dependent tensorial mobility, J. Non Newton. Fluid Mech. 11 (1982) 69–109.

[75] S.A. Khan, R.G. Larson, Comparison of simple constitutive equations for polymer melts in shear and biaxial and uniaxial extensions, J. Rheol. 31 (1987) 207–234.

[76] M. Renardy, Current issues in non-Newtonian flows: a mathematical perspective, J. Non Newton. Fluid Mech. 90 (2000) 243–259.

[77] M. Renardy, A comment on smoothness of viscoelastic stresses, J. Non Newton. Fluid Mech. 138 (2006) 204–205.

[78] M.A. Hulsen, R. Fattal, R. Kupferman, Flow of viscoelastic fluids past a cylinder at high Weissenberg number: stabilized simulations using matrix logarithms, J. Non Newton. Fluid Mech. 127 (2005) 27–39.

[79] W. Chang, F. Giraldo, B. Perot, Analysis of an exact fractional step method, J. Comput. Phys. 180 (2002) 183–199.

[80] M.A. Alves, P.J. Oliveira, F.T. Pinho, A convergent and universally bounded interpolation scheme for the treatment of advection, Int. J. Numer. Meth. Fluids 41 (2003) 47–75.

[81] S.-C. Xue, N. Phan-Thien, R.I. Tanner, Upwinding with deferred correction (UPDC): an effective implementation of higher-order convection schemes for implicit finite volume methods, J. Non Newton. Fluid Mech. 108 (2002) 1–24.

[82] C.W. Hirt, B.D. Nichols, Volume of fluid (VOF) method for the dynamics of free boundaries, J. Comput. Phys. 39 (1981) 201–225.

[83] Q. Zhang, On a family of unsplit advection algorithms for volume-of-fluid methods, SIAM J. Numer. Anal. 51 (2013) 2822–2850.

[84] J.E. Pilliod Jr., E.G. Puckett, Second-order accurate volume-of-fluid algorithms for tracking material interfaces, J. Comput. Phys. 199 (2004) 465–502.

[85] L. Jofre, O. Lehmkuhl, J. Castro, A. Oliva, A 3-D Volume-of-Fluid advection method based on cell-vertex velocities for unstructured meshes, Comput. Fluids 94 (2014) 14–29.

[86] M. Owkes, O Desjardins, A computational framework for conservative, three-dimensional, unsplit, geometric transport with application to the volume-of-fluid (VOF) method, J. Comput. Phys. 270 (2014) 587–612.

[87] C.B. Ivey, P. Moin, Conservative and bounded volume-of-fluid advection on unstructured grids, J. Comput. Phys. 350 (2017) 387–419.

[88] M. Rudman, Volume-tracking methods for interfacial flow calculations, Int. J. Numer. Meth. Fluids 24 (1997) 671–691.

[89] O. Ubbink, R.I. Issa, A method for capturing sharp fluid interfaces on arbitrary meshes, J. Comput. Phys. 153 (1999) 26–50.

[90] M. Darwish, F. Moukalled, Convective schemes for capturing interfaces of free-surface flows on unstructured grids, Numer. Heat Transfer B Fund. 49 (2006) 19–42.

[91] B.P. Leonard, The ULTIMATE conservative difference scheme applied to unsteady one-dimensional advection, Comput. Methods Appl. Mech. Eng. 88 (1991) 17–74.

[92] S.S. Deshpande, L. Anumolu, M.F. Trujillo, Evaluating the performance of the two-phase flow solver interFoam, Comp. Sci. Disc. 5 (2012) 014016.

[93] J.P. Van Doormaal, G.D. Raithby, Enhancements of the SIMPLE method for predicting incompressible fluid flows, Numer. Heat Transfer 7 (1984) 147–163.

[94] R. Tanner, Engineering Rheology, Oxford University Press, 2002.

[95] E. Mitsoulis, G.C. Georgiou, Z. Kountouriotis, A study of various factors affecting Newtonian extrudate swell, Comput. Fluids 57 (2012) 195–207.

[96] S. Claus, C.D. Cantwell, T.N. Phillips, Spectral/hp element methods for plane Newtonian extrudate swell, Comput. Fluids 116 (2015) 105–117.

[97] R.I. Tanner, A theory of die-swell, J. Polym. Sci. A Polym. Chem. 8 (1970) 2067–2078.

[98] R.I Tanner, A theory of die-swell revisited, J. Non Newton. Fluid Mech. 129 (2005) 85–87.

[99] J.Y. Yoo, H.C. Choi, On the steady simple shear flows of the one-mode Giesekus fluid, Rheol. Acta 28 (1989) 13–24.

[100] Y. Kwon, Melt fracture modeled as 2D elastic flow instability, Rheol. Acta 54 (2015) 445–453.

[101] A.I. Leonov, Nonequilibrium thermodynamics and rheology of viscoelastic polymer media, Rheol. Acta 15 (1976) 85–98.

[102] Y. Kwon, Numerical aspects in modeling high Deborah number flow and elastic instability, J. Comput. Phys. 265 (2014) 128–144.

[103] F.N. Cogswell, Stretching flow instabilities at the exits of extrusion dies, J. Non Newton. Fluid Mech. 2 (1977) 37–47.

[104] Y.W. Inn, R.J. Fischer, M.T. Shaw, Visual observation of development of sharkskin melt fracture in polybutadiene extrusion, Rheol. Acta 37 (1998) 573–582.

[105] K.B. Migler, Y. Son, F. Qiao, K. Flynn, Extensional deformation, cohesive failure, and boundary conditions during sharkskin melt fracture, J. Rheol. 46 (2002) 383–400.

[106] T.C.B. McLeish, R.G. Larson, Molecular constitutive equations for a class of branched polymers: the pom-pom polymer, J. Rheol. 42 (1998) 81–110.

[107] M.H. Wagner, P. Rubio, H. Bastian, The molecular stress function model for polydisperse polymer melts with dissipative convective constraint release, J. Rheol. 45 (2001) 1387–1412.

[108] W.M. Verbeeten, G.W. Peters, F.P. Baaijens, Differential constitutive equations for polymer melts: the extended Pom–Pom model, J. Rheol. 45 (2001) 823–843.

[109] R.S. Graham, A.E. Likhtman, T.C. McLeish, S.T. Milner, Microscopic theory of linear, entangled polymer chains under rapid deformation including chain stretch and convective constraint release, J. Rheol. 47 (2003) 1171–1200.

[110] A.E. Likhtman, R.S. Graham, Simple constitutive equation for linear polymer melts derived from molecular theory: Rolie–Poly equation, J. Non Newton. Fluid Mech. 114 (2003) 1–12.

[111] S.G. Hatzikiriakos, Wall slip of molten polymers, Prog. Polym. Sci. 37 (2012) 624–643.